Postprint of: Paszkiewicz-Gawron M., Kowalska E., Endo-Kimura M., Zwara J., Pancielejko A., Wang K., Lisowski W., Łuczak J., Zaleska-Medynska A., Grabowska-Musiał E., Stannates, titanates and tantalates modified with carbon and graphene quantum dots for enhancement of visible-light photocatalytic activity, Applied Surface Science (2020), 148425, DOI: 10.1016/j.apsusc.2020.148425

Stannates, titanates and tantalates modified with carbon and graphene quantum dots for enhancement of visible-light photocatalytic activity

Marta Paszkiewicz-Gawron[a,b], Ewa Kowalska [b], Maya Endo-Kimura [b], Julia Zwara[a], Anna Pancielejko[c], Kunlei Wang [b], Wojciech Lisowski[d], Justyna Łuczak[c], Adriana Zaleska-Medynska[a], Ewelina Grabowska-Musiał[a]

a - Department of Environmental Technology, Faculty of Chemistry, University of Gdańsk, 80-308 Gdańsk, Poland

b – Institute for Catalysis, Hokkaido University, Sapporo 001-0021, Japan

c- Department of Process Engineering and Chemical Technology, Faculty of Chemistry Gdańsk University of Technology, 80-233 Gdańsk, Poland

d - Institute of Physical Chemistry Polish Academy of Science, 01-244 Warsaw, Poland

ABSTRACT

Most efforts in heterogeneous photocatalysis are focused on development of new and stable photoactive materials efficient in degradation of various pollutants under visible-light irradiation. In this regard, the wide-bandgap perovskite semiconductors, *i.e.*, $SrTiO_3$ (titanate), $SrSnO_3$ (stannate) and $AgTaO_3$ (tantalate), were prepared by a solvothermal method, and then modified with carbon quantum dots (CQDs) or graphene quantum dots (GQDs) co-modified with erbium. The photocactivity was investigated for: (i) toluene degradation (gas phase), (ii) phenol decomposition (aqueous phase), and (iii) inactivation of *Escherichia coli* K12 bacteria. It has been found that the morphology of semiconductors depends on the synthesis conditions, resulting in the formation of spherical particles, rods and faceted particles for $SrTiO_3$, $SnSrO_3$ and $AgTaO_3$, respectively. Additionally, deposition of CQDs and GQDs/erbium has resulted in an enhancement of light harvesting, thus improved photoactivity under visible-light irradiation. Samples modified with both erbium and GQDs revealed much higher photoactivity than corresponding pristine and CQDs-modified samples. Moreover, all photocatalyst modified with GQDs and Er exhibited a significant antibacterial properties under visible light irradiation (λ>420 nm). Accordingly, it has been proposed that obtained semiconductors modified with QDs and Er are promising candidates as sustainable, clean and cheap materials for environmental purification under solar radiation.

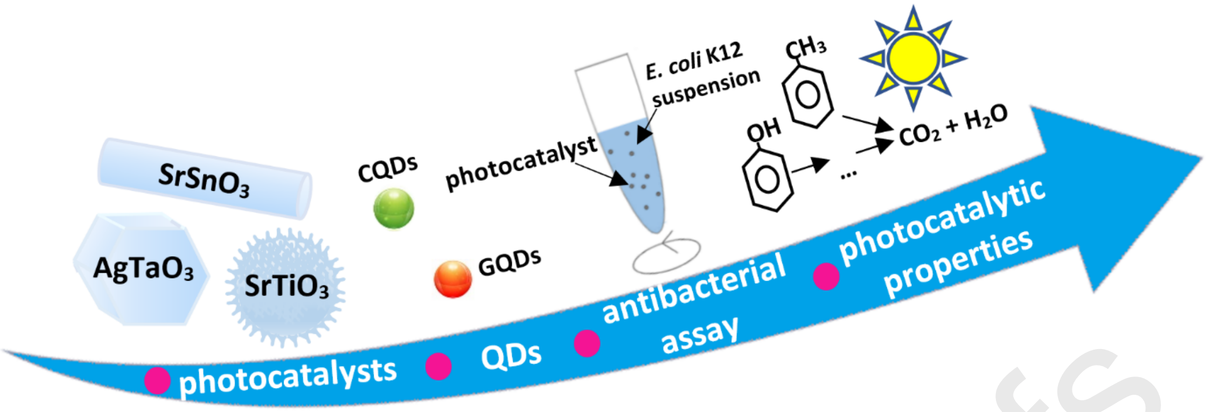

Keywords: photocatalysis, perovskites, quantum dots, graphene, action spectra analysis, antibacterial properties,

Introduction

Environmental pollution is one of the most serious problems facing humanity in recent times. Key issues on a global scale include: difficulties with access to drinking water, air pollution hampering everyday functioning, as well as over-exploitation of nonrenewable natural resources. Human activities are contributing to increasing of environmental pollution. In this regard, innovative solutions are sought to remove harmful substances from water (polluted water and wastewater) and gas phase (polluted air). Among various methods, heterogeneous photocatalysis has been considered as one of the best since under irradiation reactive oxygen species (ROS) might be formed with ability to decompose efficiently all inorganic and organic compounds even under natural solar radiation. The wide-bandgap semiconductors are used as photocatalysts for degradation of pollutants as well as for the hydrogen generation in the reaction of water-splitting [1, 2] since the wide bandgap usually results in high reactivity both for oxidation and reduction reactions. Up to now, the most popular photocatalyst, which holds a great potential due to its good chemical stability, high activity, non-toxicity (except toxicity due to the nanomaterial nature) and low-cost preparation, is titanium(IV) oxide (titania, titanium dioxide, TiO_2) [3]. However, wide bandgap (3.2 eV for anatase) causes also negative consequences , *i.e.*, TiO_2 can only be excited by ultraviolent and near-ultraviolent irradiation, which constitutes only about 4% of solar light spectrum, and thus visible range of solar spectrum (about 43%) might not be used for photocatalytic reactions. Therefore, it is necessary to design and/or further develop visible-light-active photocatalysts. Accordingly, it has been proposed that modified perovskites, e.g., titanates [4, 5], stannates [6] and tantalates [7], might be a good alternative to famous titania photocatalysts, because of their great optical properties, high photocatalytic activity and good stability. Unfortunately, most of titanates, stannates and tantalates have bandgap larger than 3.0 eV, and thus exhibit superlative properties only under UV-Vis irradiation [8]. Therefore, practical application of above mentioned perovskites is hampered by its low efficiency for utilizing of solar energy resulting in high recombination rate of photogenerated charge carries [9, 10].

To effectively utilize the sunlight, the narrowing of the band gap of semiconductors (e.g. titanates, stannates and tantalates) is required to extend its optical absorption range to the visible-light region. Accordingly, various methods for activation of wide-bandgap semiconductors towards visible-light response have been explored so far, including photosensitization [11], doping with heteroatoms [12], charge transfer (CT) interaction [13], composite semiconductors' preparation [14], modification with noble metals [15], modification with rare-earth elements [16-19], and addition of ionic liquids during the synthesis [20]. Another, innovative way to improve the photocatalytic activity under visible-light irradiation is the modification with quantum dots (QDs) [21].

The QDs-semiconductor materials have attracted interest for their unique structural, optical and electronic properties that result from the large surface-to-volume ratio and the quantum confinement effect [22]. The existence of diverse types of QDs presents a further challenge for development of various applications since each individual type possesses unique physicochemical properties. For example, carbon quantum dots (CQDs) have been recently investigated since CQDs are non-toxic, soluble in water and low-cost, as they might be even obtained from glucose, citric acid, chitosan and banana juice [23]. One type of CQDs are graphene quantum dots (GQDs) which have larger content of surface active sites and more accessible edges than graphene sheets [24]. Moreover, they exhibit excellent photostability, high biocompatibility, low toxicity and chemical inertness [25]. Therefore, it is expected to increase the photoactivity under visible light irradiation by modification of titanates, stannates and tantalates by carbon and graphene QDs. Although, the application for QDs has been rapidly increasing, there is still little known about the photocatalytic use of QDs combined with other materials (e.g., semiconductors). Furthermore, functionalized QDs might be applied for antimicrobial purposes as an alternative for traditional antibacterial drugs. Some studies on bactericidal properties of CQDs and GQDs have been performed, indicating their ability to be a bactericidal agent even under visible-light irradiation [26, 27]. Only a few studies have addresses antimicrobial effects of QDs-modified semiconductors [28-33].

Furthermore, additional modification of semiconductors by erbium ions (besides carbon QDs) may provide the materials with higher absorption ability and photocatalytic performance [34-36]. Modification of semiconductors with lanthanides (e.g. erbium) has been taken into consideration due to their significant role in altering the absorption edge of semiconductors, because of the absorption of low-energy photons (up-conversion properties) [37]. The lanthanide ions have strong ability to form complexes with various compounds such as acids, alcohols, aldehydes and amines through their 4f orbitals. Therefore, various organic pollutants might be adsorbed on the surface of lanthanide-modified semiconductors. There is a lack of information about application titanates, stannates and tantalates doped/modified with CQDs-Er for degradation of water pollutants.

In view of this, for the first time, a synthesis of highly Vis-photoactive stannates, titanates and tantalates modified with CQDs, and GQDs co-modified with erbium (0.5 mol.%) has been performed. The effect of the QDs and Er on the structural and optical properties, and the photocatalytic activity of $SrTiO_3$, $AgTaO_3$ and $SrSnO_3$ has been investigated for both degradation of chemical and microbiological pollutants.

1. Materials and methods

All reagents that were used in the experiments were of analytical purity and used without further purification. Titanium(IV) butoxide (97%), titanium(IV) chloride (98%), tantalum chloride (99.9%), hexadecyltrimethylammonium bromide (CTAB) (≥ 98%) from Sigma-Aldrich (Darmstadt, Germany), strontium nitrate (99%), silver nitrate (pure p.a.) from POCh S.A. (Gliwice, Poland), ethylene glycol (99%) from Chempur (Piekary Śląskie, Poland), sodium hydroxide (pure p.a.) and ethanol (99.8%) from STANLAB Sp. J. (Lublin, Poland) were used for the synthesis of the semiconductors.

1.1. Preparation of semiconductors: $SrTiO_3$, $SrSnO_3$ and $AgTaO_3$

The wide-bandgap semiconductors, *i.e.*, $SrTiO_3$ (1), $SrSnO_3$ (2) and $AgTaO_3$ (3), were prepared by solvothermal method. (1) **$SrTiO_3$**: the titanium(IV) butoxide (TBOT) in an amount of 1.7 g was dissolved in 25 mL of ethylene glycol by vigorous stirring for 15 min. In the next step, 10 mL (0.5 M) of $Sr(NO_3)_2$ was added dropwise to the solution. Then, 5 mL of NaOH aqueous solution (5 M) was slowly added under stirring during *ca.* 10 min. (2) **$SrSnO_3$**: 2.11 g $Sr(NO_3)_2$, 2.79 g $SnCl_4 \cdot H_2O$ and 0.55 g CTAB were dissolved in 30 mL of water under stirring. Then, the mixture was adjusted to pH = 13 with 1 M NaOH. (3) **$AgTaO_3$**: 0.95 g $AgNO_3$ and 2 g $TaCl_5$ were dissolved in 120 mL of ethylene glycol under stirring.

The obtained suspensions (1, 2 and 3) were transferred into Teflon-lined stainless-steel autoclaves and heated at 180°C for 24 h. After cooling to room temperature, the precipitates were collected, washed with deionized water and ethanol several times, and dried overnight at 60°C. In the case of $SrSnO_3$ and $AgTaO_3$, the obtained powders were calcined at 800°C for 4 h (temperature rise of 3°C/min).

1.2. Preparation of quantum dots (GQDs-Er and CQDs)

Graphene QDs were prepared as follows: 2 g of citric acid was heated at 200°C for 30 min till the colourless citric acid solids turned into orange liquid. Then, 100 mL of NaOH (10 mg/mL) was added dropwise to the orange liquid under continuous stirring, which was necessary to keep the solution homogenous. Next, pH value of the solution was adjusted to 7 with HCl [38]. Then, the appropriate amount of erbium(III) nitrate pentahydrate $Er(NO_3)_3 \cdot 6H_2O$ was added to the above mixture. The molar concentration of erbium was 0.5 mol.%. The solution was mixed for 30 min. The prepared GQDs-Er solution was used as stock solution and stored at 4°C.

Carbon QDs were prepared by hydrothermal method. 30 g of citric acid and 30 g of urea were dissolved in 100 mL of deionized water. The obtained solution was transferred into the Teflon-lined stainless steel autoclave and heated at 180°C for 5 h [39]. After cooling to room temperature, a brown aqueous solution was obtained. Large particles were removed by centrifugation, and remaining solution with carbon QDs was used as stock solution.

1.3. Preparation of semiconductor-QDs composites

In order to connect QDs with the semiconductor matrix, the physical adsorption method followed by calcination was used. Semiconductor powder (1.2 g), ethanol (30 mL) and QDs solution (7 mL) were placed in a beaker. The suspension was stirred for 24 h at room temperature with a magnetic stirrer at a speed of 500 rpm. Then, the samples were dried at 60°C and calcined at 300°C for 1 h.

1.4. Characterization of the photocatalysts

The crystalline structures and lattice parameters of the prepared samples were confirmed by X-ray diffractometer Rigaku MiniFlex 600 (Rigaku, The Woodlands, TX, USA) system equipped with a copper target. The morphology of $SrTiO_3$ semiconductors was analysed by scanning electron microscopy (SEM) using a Hitachi Microscope HD2000, as well as transmission electron microscopy (STEM-EDX, FEI Europe, model TecnaiF20 X-Twin). Measurement of absorption properties (diffuse reflectance spectra, DRS) was performed with the Shimadzu MSP-2450 spectrometer equipped with an integrating sphere, and $BaSO_4$ was used as a reference. Measurement of photoluminescence properties (fluorescence spectra) was completed with the HITACHI F-4500 spectrometer. The surface composition was analysed by X-ray photoelectron spectroscopy (XPS) using a PHI 5000 VersaProbe (ULVAC-PHI) spectrometer with monochromatic Al Kα irradiation (hν = 1486.6 eV) from an X-ray source operating at 100 µm spot size, 25 W and 15 kV. The "as prepared" semiconductors were analyzed using a modified PREVAC [https://www.prevac.eu/en/2,offer/36,sample-holders,3.html] sample holder (standard sample holder equipped with a plate adaptor of powder holding containing a cylinder pocket, 3 mm diameter, 1 mm depth). The high-resolution (HR) XPS spectra were recorded with the hemispherical analyser at the pass energy of 23.5 eV, the energy step of 0.1 eV and the photoelectron angle of 45° with respect to the surface plane. Charge compensation was achieved using a PHI's patented dual beam charge neutralization system [40]. Casa XPS software was used to evaluate the XPS data. The binding energy (BE) scale of all detected spectra was referenced by setting the BE of C 1s signal to 284.8 eV. The BET (Brunauer–Emmett–Teller) surface area and pore size of the photocatalysts were measured by a QuantaChrome Instruments, 6AG/HOB. All samples were degassed at 200°C prior to nitrogen adsorption measurements. The BET surface area was determined by the multipoint method using the adsorption data in the relative pressure (P/P_0) range of 0.05–0.3. The Raman spectra were measured with a Thermo Scientific DXR Smart Raman spectrometer with a 532 nm laser as the excitation source under ambient conditions. Fourier-transform infrared spectroscopy (FTIR) analysis was performed on Nicolet iS10 FTIR spectrometer in the scan range of 500 – 4000 cm^{-1} as the diffuse reflectance for powder samples (by rarefying 5% of the photocatalysts in KBr) and by ATR mode for liquid sample of pristine CQDs and GQDs with a resolution of 8 cm^{-1} at room temperature.

1.5. Measurement of photocatalytic activity for toluene degradation in a gas phase

Photocatalytic activity of the prepared samples was determined in the process of air cleaning from volatile organic compounds (VOC). Toluene was used as a model air contaminant. The photocatalytic activity tests were carried out in a flat stainless steel reactor (30 cm^3) [41]. The reactor was equipped with a quartz window, tow valves and septa. An array of 25 LEDs (λ_{max}= 415 nm, 63 mW per diode) was used as an irradiation source. Measured light flux (in the range from 400 to 430 nm) was 10.5 mW cm^{-2} (Hamamatsu, Japan UV Power meter, model C9536-01). Glass plate (20 mm × 20 mm) coated with the layer of photocatalyst was placed at the bottom of the reactor, followed by closing the reactor with quartz window. Subsequently, the gas mixture was passed through the reaction space for 1 min. After closing the valves, the reactor was kept in dark for 30 min to achieve adsorption/desorption equilibrium. A reference sample was taken just before starting irradiation. The analysis of toluene concentration in the gas phase was performed using gas chromatograph (SCHIMADZU, GC 2010) equipped with flame ionization detector (FID) and Phenomenex capillary column (30 mm x 25 mm, 0.5 µm). The samples (200 µL) were dosed with a syringe. Helium was used as a carrier gas (1 mL min^{-1}). To estimate toluene loss due to adsorption on the photocatalyst surface, the experiments in dark were also proceeded, where *ca.* 12% decrease in toluene concentration was obtained.

1.6. Measurement of photocatalytic activity for phenol degradation in an aqueous phase– action spectra (AS) analysis

The action spectra (AS) analyses for phenol degradation in an aqueous phase were also conducted. Photocatalyst powder (15 mg) was suspended in an aqueous solution (3.0 mL) containing phenol (C_0 = 20 mg · L^{-1}) and placed in a rectangular quartz cell (10 mm square and 50 mm in height), then irradiated at monochromatic wavelengths for 60 min using a diffraction grating-type illuminator (Jasco, CRM-FD) equipped with a 300-W xenon lamp (Hamamatsu, C2578-02). The light intensity was measured by an optical power meter (HIOKI 3664). During the experiments, the suspension was continuously stirred, and a portion (0.2 mL) of the reaction mixture was withdrawn every 20 min with a syringe, filtered by a syringe filter (Ø = 0.2 µm, Whatman, Mini-UniPrep) to remove photocatalyst particles, and injected to high-performance liquid chromatograph (HPLC). The HPLC system was equipped with a WAKOSIL-II SC18 AR reversed-phase column (250 × 4.6 mm) with a mobile phase of acetonitrile (29.5%), water (70%) and phosphoric acid (0.5%), and analysis parameters were fixed at 1 mL min^{-1} of a flow rate and UV detector at 254 nm.

1.7. Antimicrobial properties

Pristine and modified semiconductors (50 mg) were dispersed in 5 cm^3 *Escherichia coli* (*E. coli*) K12 ATCC29425 suspension in a sterile sodium chloride aqueous solution (8.5 g dm^{-3}) in a glass test tube, and irradiated by a xenon lamp (CX-04E, Eagle Engineering, Ltd., Japan) equipped with cut-off filter (λ>420 nm) and a cold mirror in thermostated water bath under continuous stirring (using a magnetic stirrer at speed of 500 rpm) at 25°C. The distance between the solution and the light source was fixed at *ca.* 15 cm. The radiant flux was monitored with a spectroradiometer (USHIO, USR-45) and equaled to 20.0 mW cm^{-2}. The process was carried out for 3 h for each sample. Samples were collected at 0.5, 1.0, 2.0 and 3.0 h. The content of photocatalyst and bacteria was adjusted, according to the previous findings [42]. The control experiments in darkness and for NaCl solution were also performed. Serial dilutions (10^{-1} to 10^{-6}) were prepared in saline solution (0.85%). The samples were placed on Plate Count Agar (Becton, Dickinson and Company, Franklin Lakes, NJ, USA), the plates were incubated for 20 h at 37°C (ETTAS EI-450B incubator), and then the colony forming unit (CFU x cm^{-3}) was calculated. The procedure for determining antibacterial activity is shown schematically in Figure 1.

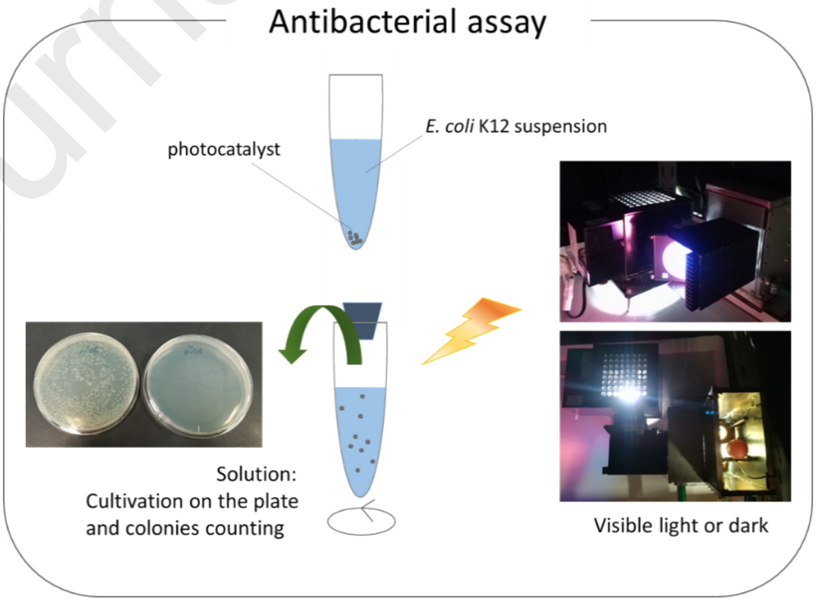

Figure 1 Scheme of antibacterial assay against *E. coli* procedure.

2. Results and Discussion

Solvothermal synthesis performed at 180^{o}C was applied for preparation of three types of perovskites, namely $SrTiO_3$, $SrSnO_3$ and $AgTaO_3$. The materials were then modified with CQDs, and with GQDs co-modified with erbium ions. Firstly, formation of graphene and carbon QD was confirmed by UV-Vis absorption and fluorescence spectroscopy. Then, the modified perovskites were analysed in respect to the crystal structure, morphology, optical and surface properties and the photocatalytic activity, as discussed below.

2.1. Characteristics of GQDs-Er and CQDs

The optical properties of GQDs were investigated by UV-Vis absorption and fluorescence spectroscopy (Fig. 2). The absorption peak at 365 nm (Fig. 2a) correlates well with π-π* transition of C=C [43]. The maximal emission was detected at *ca.* 465 nm, independently on the excitation wavelength, revealing excitation-independent fluorescent properties, as previously reported [38]. It means that the emission wavelength of GQDs was stable, with the excitation wavelength ranging from 350 to 400 nm (Fig. 2b). The photograph of the obtained solution taken under 395 nm LED irradiation (Fig. 2c (left)) confirms the blue fluorescence of GQDs (no emission for irradiated water (Fig. 2c (right)), which is consistent with the spectrum shown in Fig. 2b (excitation with UV irradiation gives the emission in the visible irradiation range). Peaks indicating the erbium content were not noticeable in the spectrum probably because of too low content of this element in the tested samples. The presence of erbium in the samples was confirmed by other techniques, which is discussed later in the article.

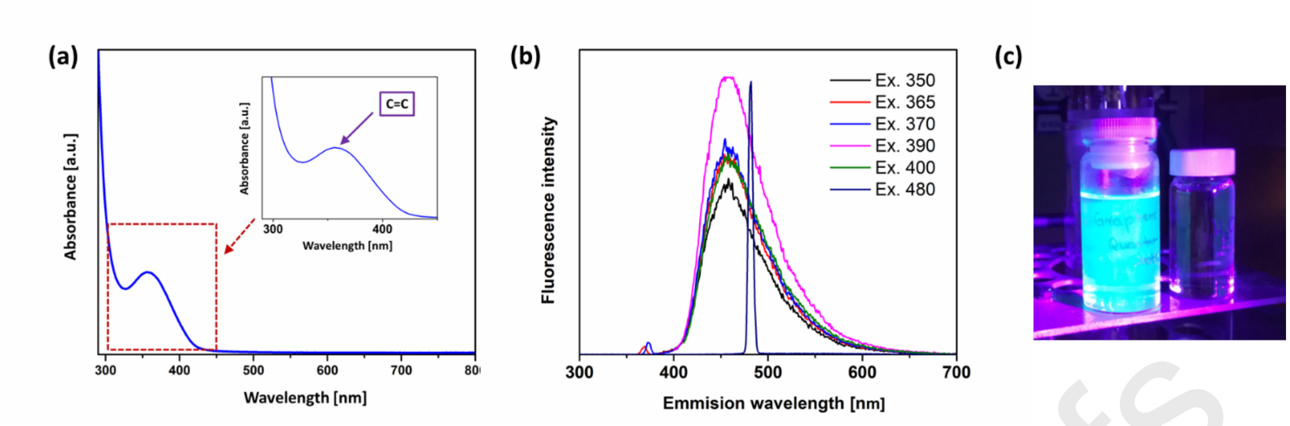

Figure 2 Optical properties of GQDs_Er: (a) UV-Vis absorption spectrum; (b) fluorescence excitation and emission spectra; and (c) photographs under UV irradiation for: GQDs (left) and water as a reference sample (right).

Carbon QDs showed absorption under the visible range of irradiation from ~ 430 to 500 nm and at 650 nm (Fig. 3a). The first peak might originate from π-π* transition of C=C [43]. The phenomenon of the second wide peak (at 650 nm) is presumably related to the presence of carbon dots dispersed in the solution, as also observed by other scientific groups. For comparison, Li *et al.* observed a well-defined, strong absorption band at about 700 nm for carbon nanodots prepared *via* hydrothermal method from citric acid and urea [44]. Wang *et al.* noticed the absorption peak at 530 nm from CQDs, claiming that it indicated the high conjugation and high quality of CQDs [45]. The photoluminescence (PL) spectra, shown in Fig. 3b, indicate that CQDs emit in blue and green ranges, depending on the excitation wavelengths, *i.e.*, PL from nearly 450 to 550 nm after excitation at 300-500 nm, respectively. The bathochromic shift in the emission wavelength correlates with excitation wavelengths, *i.e.*, the longer excitation wavelength is, the longer is the emission wavelength. It should be pointed out that such spectra are typical for CQDs [46, 47]. The maximum photoluminescence intensity with emission at 450 nm was observed when CQDs were excited at 400 nm. The broad emission bands revealed the complex mechanism of the CQDs photoluminescence [48], as already reported [49, 50].

Both types of QDs (graphene with erbium and carbon) did not revealed the up-conversion properties, *i.e.*, they could not emit ligth at shorter wavelenghts (e.g., UV) after absorption of light at longer wavelenghts (*i.e.,* Vis or NIR). It should be pointed that the addition of 0.5% erbium did not cause the appearance of up-conversion. Nevertheless, decorating the semiconductors with GQDs/Er^{3+} and CQDs has increased the photocatalytic activity, as discussed in detail in the further sections of this article.

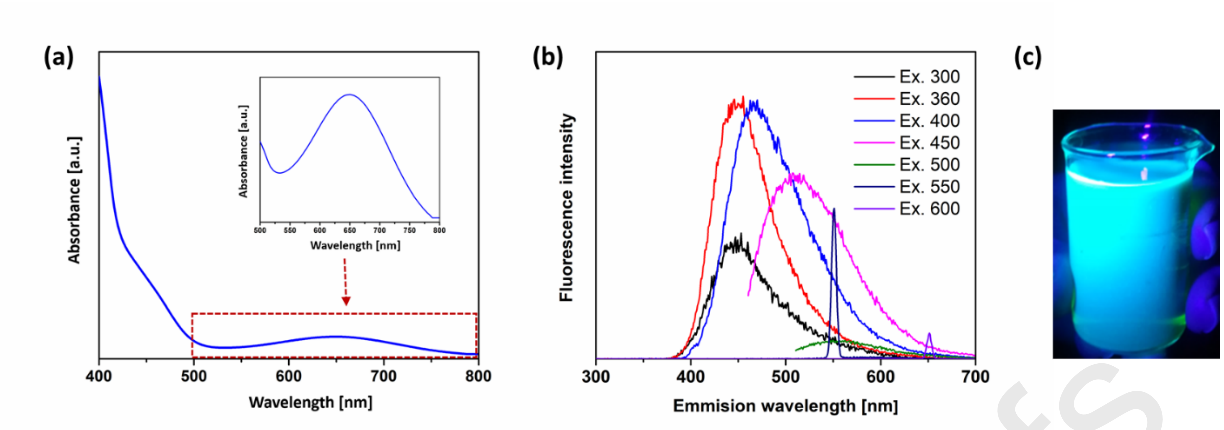

Figure 3 Optical properties of CQDs: (a) UV-Vis absorption; (b) fluorescence excitation and emission spectra; (c) picture under UV irradiation of carbon quantum dots (CQDs).

In case of carbon quantum dots the up-conversion fluorescence are frequently cited as an important feature. However we can find in the literature many examples of contradicting this thesis. Many research groups obtained carbon QDs which couldn't exhibit the transformation of visible light (or NIR) to UV light [44, 45, 47, 49, 51]. Additionally, very interesting article was published in Chemical Communications [52]. The authors said that the upconversion fluorescence has been often cited as an important feature in carbon nanodots (CNDs) and graphene quantum dots (GQDs); and some mechanisms and potential applications have been proposed. Contrary to such a general belief, they demonstrated in this report no observable upconversion fluorescence based on five different synthesized CNDs and GQDs. They confirmed that the so-called upconversion fluorescence actually originates from the normal fluorescence excited by the leaking component from the second diffraction in the monochromator of the fluorescence spectrophotometer. Upconversion fluorescence can be identified by measuring the excitation intensity dependence of the fluorescence [52]. Also in the following article, the authors deny the up-conversion properties of CQDs (the title of that paper is: A misunderstanding about upconversion luminescence of carbon quantum dots) [53].

2.2. Characteristics of semiconductor-QDs samples

2.2.1. The XRD and BET analyses

The XRD patterns of the pristine and modified samples are shown in Fig. 4. It is clear that all diffraction peaks of pristine $SrTiO_3$, indexed to cubic crystal system, are observed at near 22.8°, 32.4°, 40.1°, 46.6°, 50.1°, 57.8°, 67.9°, and 77.1°, as presented in Fig. 4a. Characteristic peaks of trigonal $AgTaO_3$ are noticed at *ca.* 22.9°, 32.3°, 46.1°, 54.1°, 57.6°, 67.7° and 76.8° (see Fig. 4b) for both pristine and modified samples. However, additional peaks have also been detected, such as $Ag_2Ta_4O_{11}$ and Ta_2O_5 (Figure 4b). The additional peaks corresponding to Ta_2O_5 and $Ag_2Ta_4O_{11}$ observed in Figure 4b might come due to occur additional side reactions. We assume that much more drastic cleaning and calcination conditions (such as different in properties cleaning solutions, higher pressure and temperature) could completely remove the rest compounds. For the $AgTaO_3$_GQDs_Er sample we found an intensive peak at around 39° ascribed to a metallic silver (111) [54-57]. We suspected that it might be a result of the synthesis conditions and coexistence of two metals, silver and erbium. The remaining characteristic peaks for metallic silver (i. e. (200) at around 44.3°, (220) near 64.5° and (131) 77.4° coincide with that one's corresponding to $AgTaO_3$ were observed [54-57].

The diffraction patterns, assigned to orthorhombic $SrSnO_3$ with peaks at *ca.* 22.1°, 25.3°, 31.5°, 36.7°, 45.0°, 50.7°, 52.1°, 55.9°, 65.5°, 66.4°, 70.0° and 74.4°, are presented in Fig. 4c. The average crystalize sizes calculated using Scherrer equation were equalled to 32.5, 20.1 and 8.81 nm for $AgTaO_3$, $SrSnO_3$ and $SrTiO_3$, respectively. Furthermore, the addition of quantum dots to the reaction environment resulted in significant changes in crystallize sizes. The refined lattice parameters a, b and c as well as cell volume are summarized in Table 1. The influence of CQDs and GQDs/Er^{3+}, for both $SrTiO_3$ and $AgTaO_3$ samples led to a decrease in the average crystallize sizes, from 8.4 nm to 8.0 and 3.6 for pristine sample, $SrTiO_3$_CQD and $SrTiO_3$_GQDs_Er, respectively, and from 32.5 nm to 23.1 and 16.5 nm, for pristine sample, $AgTaO_3$_CQDs and $AgTaO_3$_GQDs_Er, respectively. On the other hand, the increase in the crystallize sizes after addition of quantum dots to $SrSnO_3$ was observed, *i.e.*, from 20.9 nm for pristine sample to 28.9 and 24.5 nm for $SrSnO_3$_CQDs and $SrSnO_3$_GQDs_Er, respectively. Accordingly, it has been proposed that the second calcination used for preparation of the QDs-composites caused further growth of $SrSnO_3$ crystallites. However, in the case of $SrTiO_3$ and $AgTaO_3$ composites an opposite effect was observed. Therefore, it might be assumed that the initial presence of the amorphous phase in both pristine semiconductors is a reason of this phenomenon, *i.e.*, during their crystallization fine NPs are formed, and thus the resultant sizes (average/mean) are smaller after second calcination (higher crystallinity of samples). The specific surface areas of as-prepared samples, calculated based on the BET isotherms, are listed in Table 1. The results clearly showed that the addition of quantum dots to the reaction environment led to decrease in the specific surface area, probably because of the pore blocking by QDs. Similar results have already been reported by Stengl *et al.* for TiO_2-graphene nanocomposite [58]. They reported that the increase of graphene nanosheets content in the nanocomposite led to the decrease of the specific surface area.

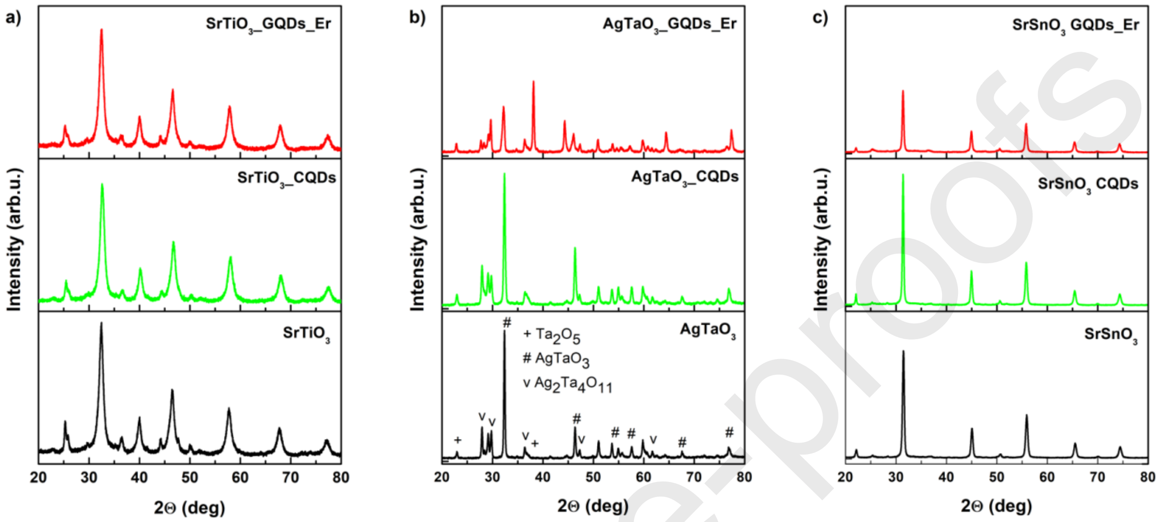

Figure 4 XRD patterns of the pristine and modified samples of: (a) $SrTiO_3$; (b) $AgTaO_3$; (c) $SrSnO_3$.

Table 1 Crystallographic properties and BET area of the obtained samples.

Sample label	Type of QDs	Crystallite size (Å)	Cell parameters (Å)		Cell volume (Å³)	BET surface area [m² · g⁻¹]
			a=b	c		
$SrTiO_3$	-	84	3.8990	3.8990	59.273	107.9
$SrTiO_3$_CQDs	C	80				106.8
$SrTiO_3$_GQDs_Er	G	36				82.95
$AgTaO_3$	-	325	5.5281	13.7159	363.00	0.91
$AgTaO_3$_CQDs	C	231				0.74
$AgTaO_3$_GQDs_Er	G	165				0.83
$SrSnO_3$	-	209	5.5281	8.0640	262.643	13.7
$SnSrO_3$_CQDs	C	289				8.45
$SnSrO_3$_GQDs_Er	G	245				8.45

2.2.2. Morphology

The morphological properties of GQDs/Er-modified perovskites ($AgTaO_3$, $SrSnO_3$ and $SrTiO_3$) were studied by SEM and TEM analyses (Fig. 5). It was found that $AgTaO_3$_GQDs_Er formed faceted particles with width and length of *ca.* 300 and 870 nm, respectively (Fig. 5a). It is worth to noticed that each of the crystals consisted of several overlapping thin layers of 4-8 nm thickness and irregularly shaped particles of about 4-15 nm on the surface. (Fig. 5b-c). These irregular particles suggest the presence of GQDs on the surface of the perovskite. The enlarged image (Fig. 5d) of $AgTaO_3$_GQDs_Er revealed the longitudinal rods/sheets of about 1 nm thickness, indicating the presence of graphene. The typical images of $SrSnO_3$, *i.e.*, in the form of porous rods with a length of 3-10 µm and a diameter from 0.5 to 1.5 µm, are shown in Fig. 5 e-f. Kim *et al.* reported the synthesis of $SrSnO_3$ particles of similar morphology *i.e.*, rod-like particles with a square base of 0.7 - 1.5 µm and a height of approximately 2.0 - 3.0 µm [59]. The differences in the size might result from the different preparation routes than that in our experiments (different precursor - $SrCl_2 \cdot 6H_2O$, hydrothermal reaction at 200°C for 18 h, calcination at 600°C for 6 h). SEM images for $SrTiO_3$ (Fig. 5g-h) revealed the presence of particles with a size from 300 to 800 nm. What is more, they were highly aggregated, which is in line with our previous studies [5]. These particles consisted of thin petals with an average thickness of about 10 nm. Moreover, non-uniform jagged at the edge could be observed on their surface. Unfortunately, in all obtained semiconductors it is difficult to indicate (on the basis of SEM and TEM) the presence of erbium on the surface of perovskites, due to its low content in the samples.

In addition, EDS mapping was carried out for three selected samples ($SrSnO_3$_GQDs_Er, $AgTaO_3$_GQDs_Er, $SrSnO_3$_CQDs) to confirm the presence of QDs (Fig. 6). The EDS analysis confirmed the presence of signals from C, Sr, Sn, Ta and Ag from the above-mentioned composites.

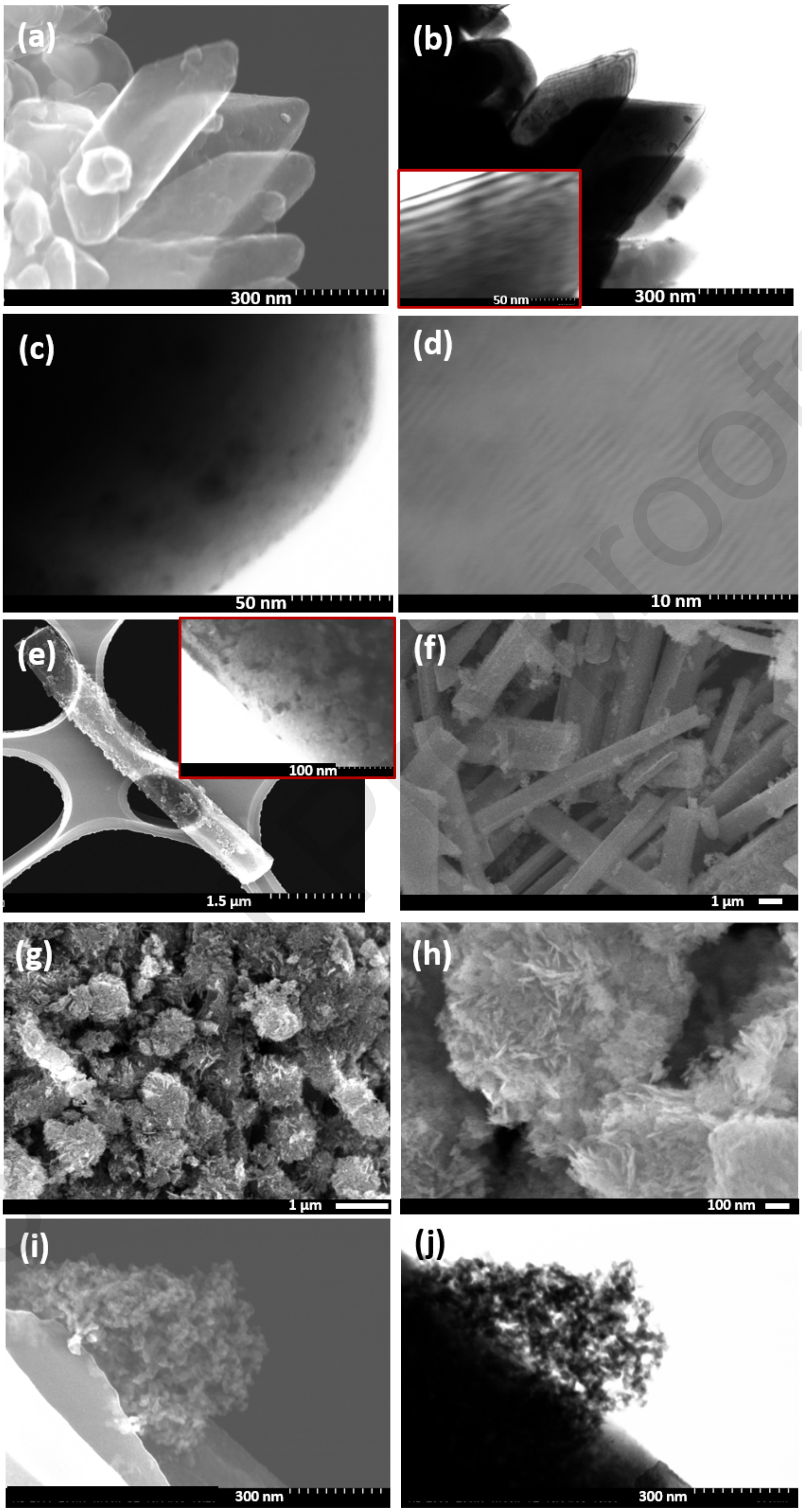

Figure 5 STEM images of the prepared samples: $AgTaO_3$_GQDs_Er: SEM (a) and TEM (b-d) images; $SrSnO_3$_GQDs_Er: TEM (e) and SEM (f) images, $SrTiO_3$_GQDs_Er: SEM (g-h) images; and $SrSnO_3$_CQDs: SEM (i-j).

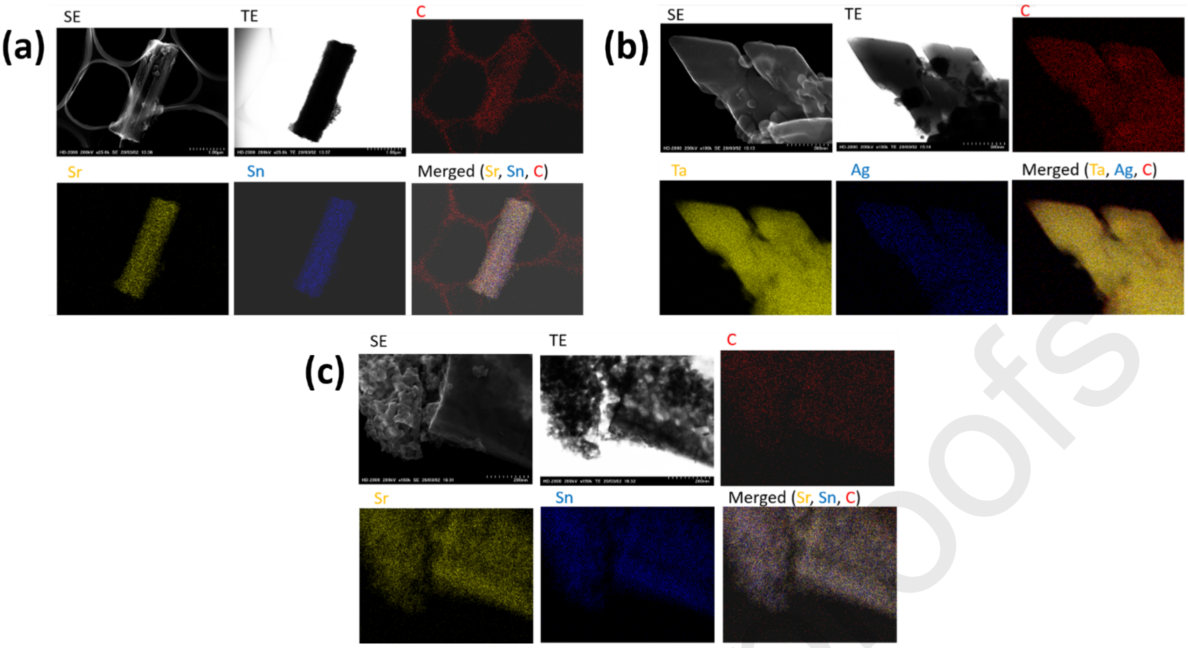

Figure 6 STEM/EDS mapping for three selected samples: (a) $SrSnO_3$_GQDs_Er, (b) $AgTaO_3$_GQDs_Er, (c) $SrSnO_3$_CQDs.

2.2.3. The XPS analysis

The elemental composition of the surface of pristine and modified $SrTiO_3$, $AgTaO_3$, $SrSnO_3$ was determined by XPS, and results are collected in Table 2. The chemical character of elements in the $SrTiO_3$, $AgTaO_3$ and $SrSnO_3$ samples was identified in HR XPS spectra, presented in Fig. 7, Fig. 8 and Fig. 9, respectively. In the case of $SrTiO_3$ (Fig. 7), two states of strontium in Sr 3d spectra, *i.e.*, Sr $3d_{5/2}$ peaks at 132.8 and 133.6 eV, were assigned to $SrTiO_3$ and $SrCO_3$ species, respectively [60], and the Ti $2p_{3/2}$ signals, located at 458.3 eV and 456.7 eV, are characteristic for $SrTiO_3$ and Ti^{3+}species, respectively [60-62]. The $AgTaO_3$ samples were identified by Ag 3d and Ta 4f spectra (Fig. 8). The Ag $3d_{5/2}$ peak at 368.0 eV described well the pristine $AgTaO_3$ and the main Ta 4f signals (Ta $4f_{7/2}$ close to 26.0 eV) identify the $AgTaO_3$ compounds [63]. The $SrSnO_3$ composites were well characterized by the Sr 3d and Sn 3d spectra (Fig. 9). The Sr $3d_{5/2}$ signals at 132.7 and 133.7 eV, indicated two states of strontium assigned to $SrSnO_3$ and $SrCO_3$, respectively [60, 64], and the Sn $3d_{5/2}$ signal located at 486.3 eV is attributed to $SrSnO_3$ [64]. The successful erbium doping is confirmed by Er 4d spectra recorded for all samples containing graphene QDs and erbium. However, for $SrTiO_3$_GQDs_Er and $SrSnO_3$_GQDs_Er samples, the Er 4d spectra were partially overlapped with Sr-loss peaks (see Fig. 7 and Fig. 9).

To confirm effective modification of $SrTiO_3$, $AgTaO_3$ and $SrSnO_3$ with CQDs and GQDs, the C 1s spectra were analysed for all samples. The deconvoluted C 1s spectra revealed four fractions, denoted as C1-C4, and corresponding to C1 – C-C bonds; C2 – C-O; C3 – C-Cl/C=O; C4 – O-C=O/Na_2CO_3 (Table 3). Accordingly, it was found that the C4 fraction was higher in all modified samples than that in pristine semiconductors. Moreover, the ratio (C3+C4)/(C1+C2), representing the relative carbon fraction distribution, evidently was higher in carbon-containing samples (Table 3). However, it should be noted, that all samples co-modified with GQDs and Er contained significant amount of sodium originated from precursors used in the preparation process (Table 2), which might also contributed to an increase in the fraction of C4 (Na_2CO_3) [60]. Moreover, it should be pointed out that all samples might be partially covered with the carbon-like compounds, being formed as a result of exposition to air after their preparation. However, evaluation of this effect is rather doubtful, because both the specific surface area and the chemical composition of pristine samples was found to be changed as a result of CQDc and GQDs_Er modification. The C1 fraction of contributed carbon species was evidently largest in all pristine samples (Table 3).

Table 2 Elemental contents in the surface layer of pristine $SrTiO_3$, $AgTaO_3$ and $SrSnO_3$ composites and the samples doped by carbon quantum dots (CQDs) as well as graphene quantum dots and erbium (GQDs_Er).

Sample label	Ag cont. at.%	Ta cont. at.%	Sr cont. at.%	Ti cont. at.%	Sn cont. at.%	O cont. at.%	Er cont. at.%	C cont. at.%	Other (Na, Cl,) cont. at.%
$SrTiO_3$	-	-	21.24	13.76	-	52.00	-	13.00	< 0.1
$SrTiO_3$_CQDs	-	-	22.90	14.65	-	57.41	-	5.04	< 0.1
$SrTiO_3$_GQDs_Er	-	-	15.84	9.48	-	47.42	0.11	9.75	17.40
$AgTaO_3$	15.56	15.06	-	-	-	30.09	-	24.55	14.74
$AgTaO_3$_CQDs	18.89	10.76	-	-	-	21.34	-	29.99	19.02
$AgTaO_3$_GQDs_Er	3.71	4.26	-	-	-	33.05	0.98	36.34	21.66
$SrSnO_3$	-	-	16.12	-	16.45	54.76	-	12.67	< 0.1
$SrSnO_3$_CQDs	-	-	18.72	-	15.07	54.79	-	11.42	< 0.1
$SrSnO_3$_GQDs_Er	-	-	16.62	-	2.64	46.42	0.39	20.06	13.87

Table 3 The analysis of C 1s XPS spectra of pristine $AgTaO_3$, $SrTiO_3$ and $SrSnO_3$ composites and the samples doped by carbon quantum dots (CQDs) as well as graphene quantum dots and erbium (GQDs_Er).

Sample label	**C 1s fraction (%)**				**(C3+C4)/ (C1+C2)**
	C1	**C2**	**C3**	**C4**	
	C-C 284.8 eV	**C-O** 286.3 ± 0.5 eV	**-C-Cl/C=O** 287.9± 0.4 eV	**O-C=O/Na_2CO_3** 289.4± 0.3 eV	
$SrTiO_3$	49.67	32.76	0	17.57	0.21
$SrTiO_3$_CQDs	24.03	13.57	0	62.40	1.66
$SrTiO_3$_GQDs_Er	14.14	4.33	0	81.53**	4.41**
$AgTaO_3$	64.97	23.98	8.41*	2.63	0.12*
$AgTaO_3$_CQDs	53.81	21.31	21.89*	0	0.29*
$AgTaO_3$_GQDs_Er	53.43	10.06	11.44*	25.07**	0.58*/**
$SrSnO_3$	57.79	4.20	0	38.01	0.61
$SrSnO_3$_CQDs	46.80	14.40	0	38.81	0.63
$SrSnO_3$_GQDs_Er	11.71	3.24	0	85.05**	5.69**

*C-Cl; **C-Na

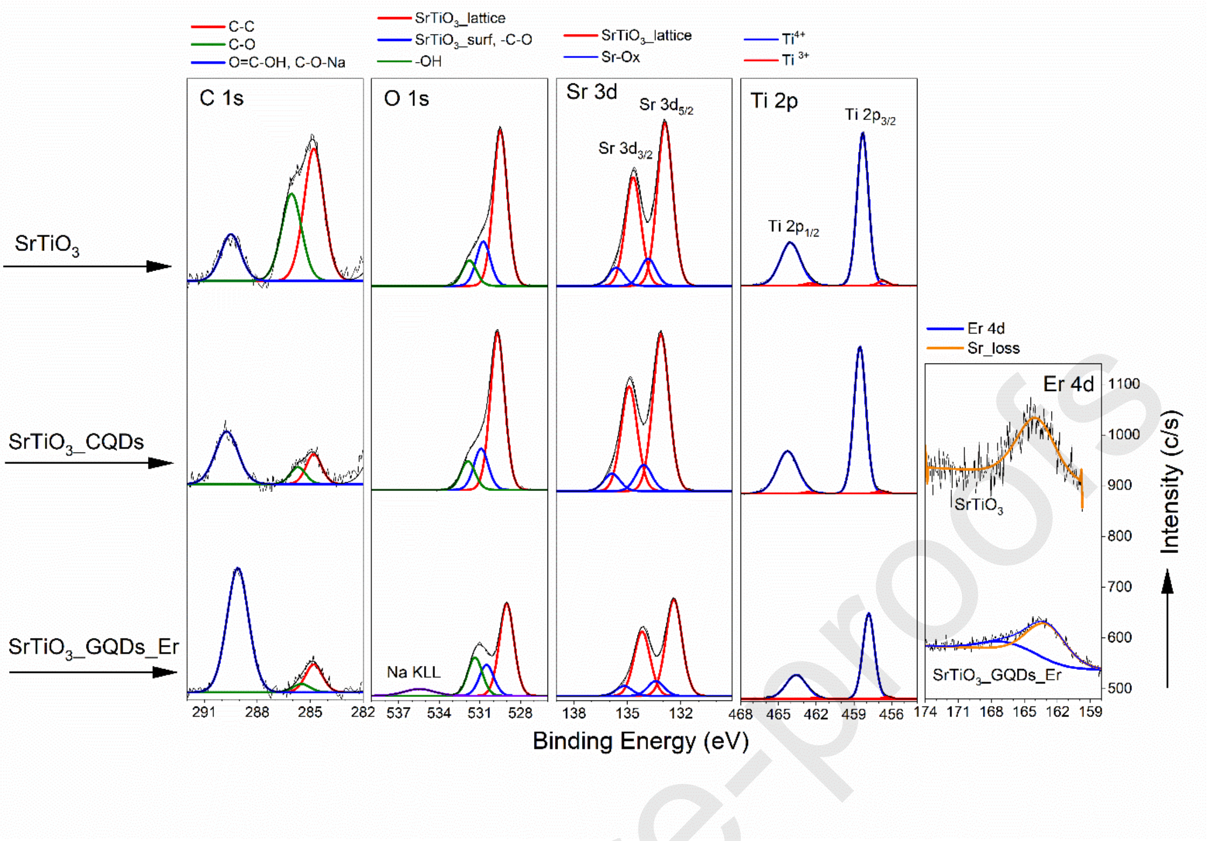

Figure 7 High resolution XPS spectra of C 1s, O 1s, Sr 3d, Ti 2p, Er 4d collected on the surface of pristine and modified $SrTiO_3$ samples.

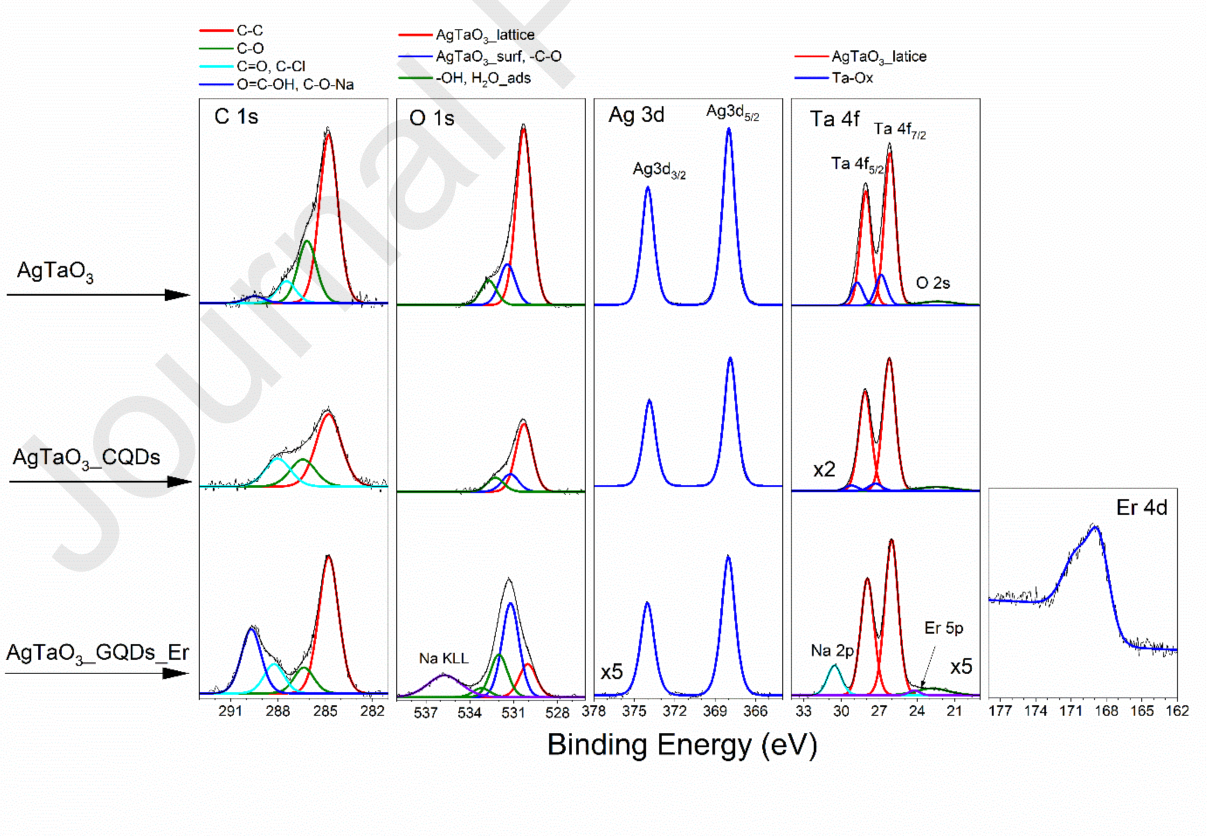

Figure 8 High resolution XPS spectra of C 1s, O 1s, Ag 3d, Ta 4f, Er 4d collected on the surface of pristine and modified $AgTaO_3$ samples.

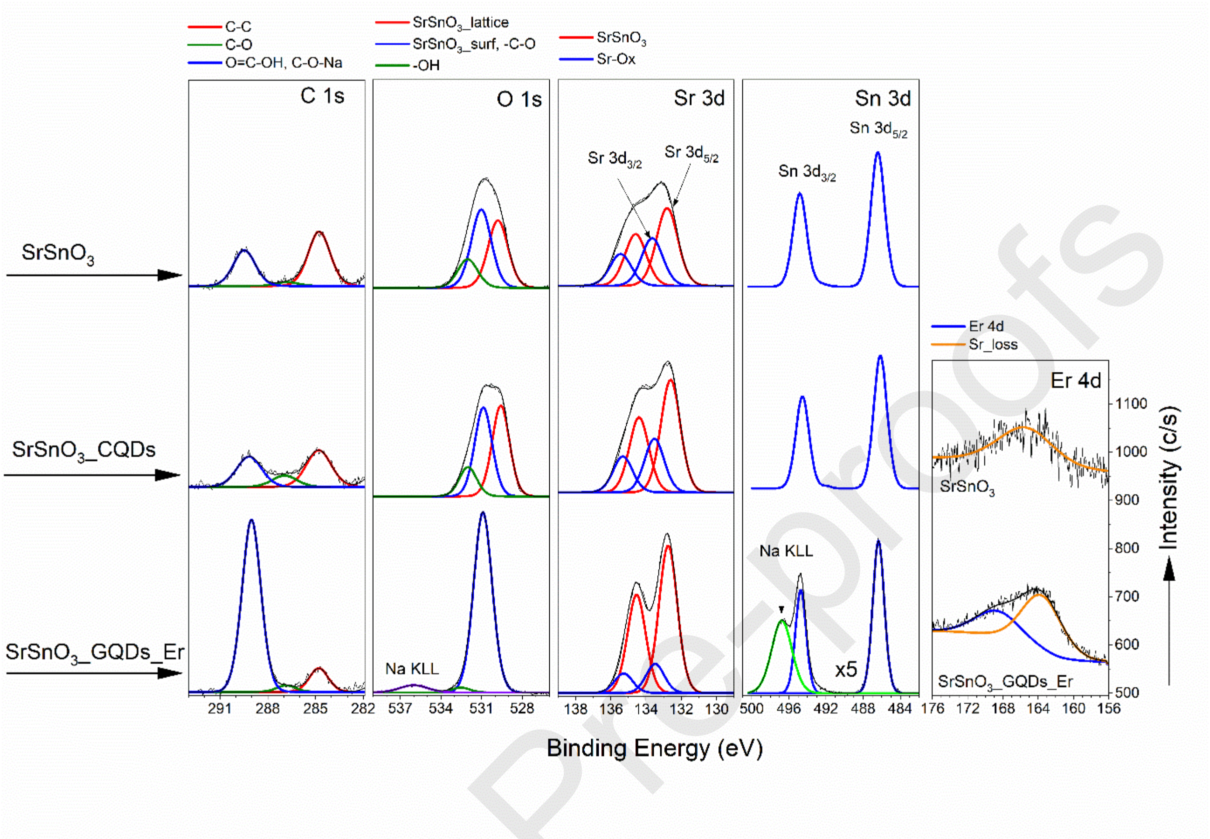

Figure 9 High resolution XPS spectra of C 1s, O 1s, Sr 3d, Sn 3d, Er 4d collected on the surface of pristine and modified $SrSnO_3$ samples.

2.2.4. The FTIR and Raman analyses of lattice vibration modes

Interfered spectra of the obtained samples are presented in Fig. 10. The strongest signal, centred at around 590 cm^{-1}, corresponds to characteristic stretching vibrations of Sr-Ti-O, and thus confirming the successful synthesis of $SrTiO_3$ (Fig. 10a). The bands in the range of 2700 – 2900 cm^{-1} were assigned to the presence of CH_3 and CH_2 symmetric vibrations in the alkyl chain, originated from the precursor (TBOT), and for the modified samples were concealed. Pristine $SrTiO_3$ in comparison with modified samples exhibited the same features but transmittance was less intense. The functional groups corresponding to the Ag-O bonds were noticed at around 690 and 820 cm^{-1} (Fig. 10b). For $SrSnO_3$, the vibrations associated to Sn-O molecular vibrations were observed at 400 - 850 cm^{-1}. The peaks appearing at 480 and 762 cm^{-1} correspond to vibrations of the O–Sn–O bridging (Fig. 10c). Besides the bands originated from metal-oxygen, in each series of the samples, the bands located in the range of 3100 – 3700 cm^{-}

^{1} and 2600 - 2700 cm^{-1}, originated from hydroxyl groups vibration, and the bands centred around 1600 – 1700 cm^{-1} were associated with O-H deformation vibrations, originated from the water adsorption on the surface of the samples. It is worth to note that the bands corresponding to both types of QDs, might be distinguished at around 1620 – 1750 cm^{-1} and 1470 cm^{-1} (see Fig. 10d). However, it is hard to distinguish the presence of CQDs and GQDs with Er ions in modified samples in comparison with the pristine ones due to overlapping of the bands. It has been assumed that the differences in the intensities might result from the preparation routes of the composites.

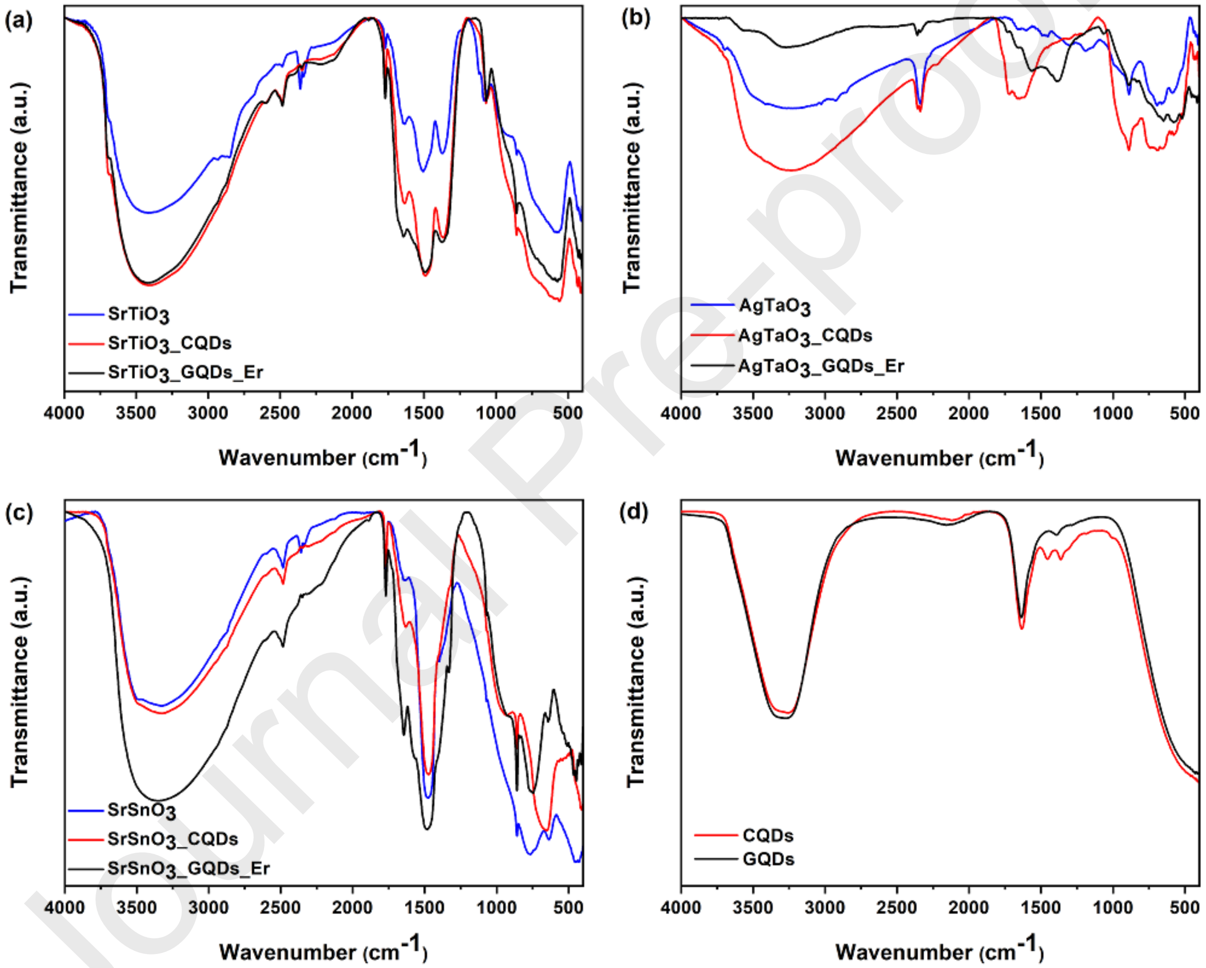

Figure 10 FTIR analysis of pristine and modified samples of: (a) $SrTiO_3$; (b) $AgTaO_3$; (c) $SrSnO_3$ and (d) pure carbon and graphene quantum dots.

Figure 11 represents three Raman spectra denoted as a – c and corresponding to the obtained semiconductors, *i.e.*, $SrTiO_3$, $AgTaO_3$ and $SrSnO_3$, respectively. Characteristic bands related to the typical vibrational modes of the as-prepared perovskites associated with metal-oxygen interaction were observed (below 600 cm^{-1} for Sr-O, at around 690 and 820 cm^{-1} for Ag-O and at 559 cm^{-1} for Sn-O, respectively). For example, several broad bands observed in the frequency range up to 600 cm^{-1} might be associated with different modes of O-Sr-O and Sr-Ti-O (see Fig. 11a). These structures arose at about 134, 175, 257 and 590 cm^{-1} for pristine as well as modified $SrTiO_3$ samples [65]. Furthermore, in the case of the $SrTiO_3$_CQDs and $SrTiO_3$_GQDs_Er samples, two additional peaks at around 1340 and 1580 cm^{-1} were observed [66, 67], probably associated with the presence of carbon and graphene quantum dots on the surface of $SrTiO_3$. As expected, the similar bands corresponding to carbon and QDs at around 1470 and 1620 cm^{-1} were also noticed for the modified $AgTaO_3$ samples (Fig. 11b). Although, different intensity of signal was noticed for the $AgTaO_3$_GQDs_Er and $AgTaO_3$_CQDs samples, the same features were observed. The spectrum of pristine $AgTaO_3$ is consistent with previous literature reports, where the functional groups corresponding to the Ag-O bonds were noticed at around 690 and 820 cm^{-1} [68]. The Raman spectrum of pristine $SrSnO_3$ demonstrated main signals, attributed to the movement of Sn-O-Sn groups, at 221 and 266 cm^{-1}. The band at 559 cm^{-1}, associated with Sn–O stretching motions, has already been reported for $SrSnO_3$ [69-71]. The spectrum analysis revealed the presence of two peaks located in the range of 1380 – 1580 cm^{-1}, associated with graphene QDs, as presented in Fig. 11c. However, analysis of $SrSnO_3$_CQDs was hard to employ, probably because of the strong reflection from the laser beam and fluorescence phenomenon preventing the measurement. Moreover, the peaks at 279, 700 and 1073 cm^{-1} could indicate $SrCO_3$, as reported previously [72].

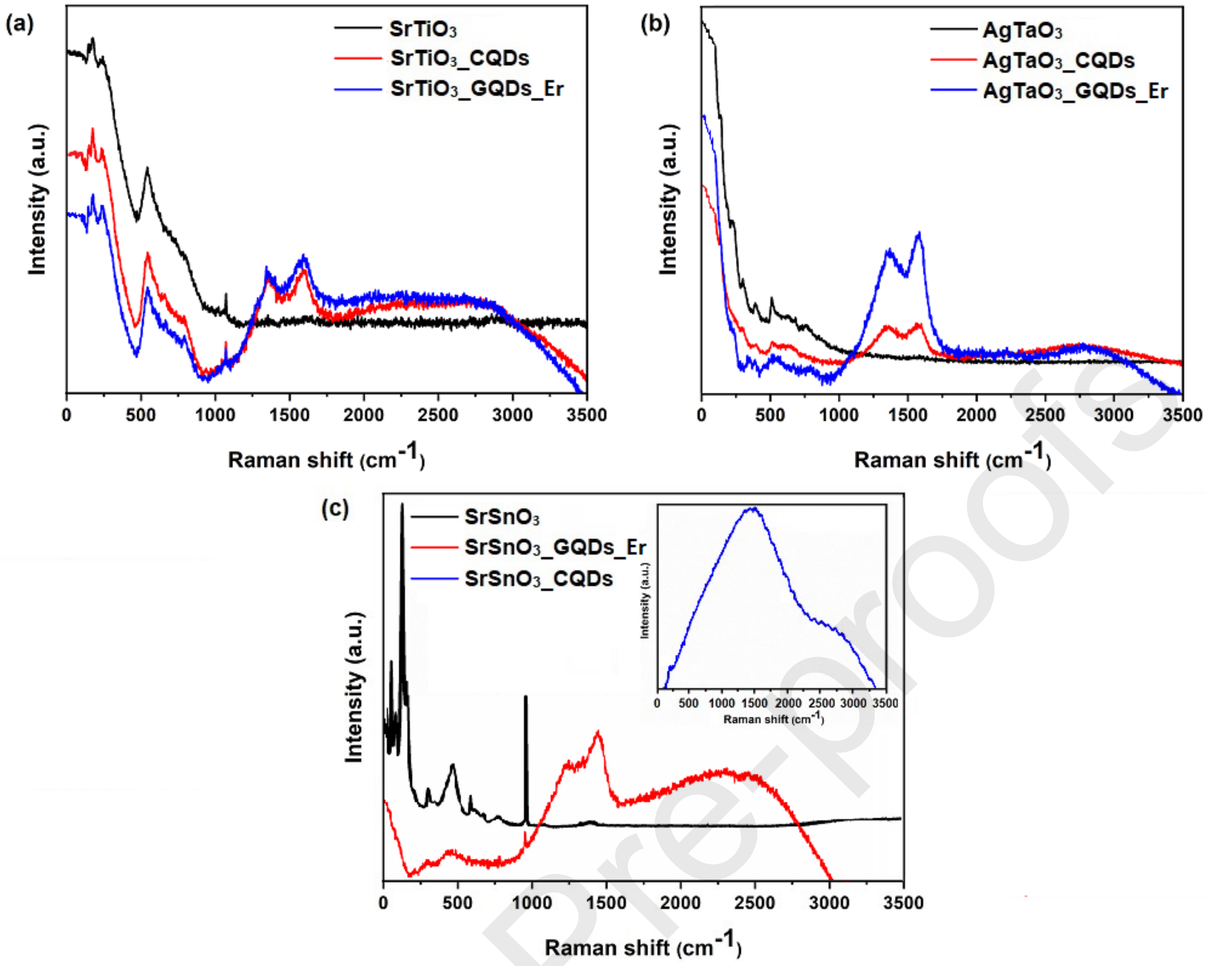

Figure 11 Raman spectra of pristine and modified samples of: (a) $SrTiO_3$; (b) $AgTaO_3$; (c) $SrSnO_3$.

2.2.5. Photoluminescence properties

The PL emission spectra of all samples were analysed in the wavelength range of 350 – 700 nm, as presented in Fig. 12. All pristine samples exhibited the highest PL intensity what suggests the highest efficiency of charge carriers' recombination. A peak at around 398 nm is attributed to the emission of band gap transition, originated from the recombination of photoexcited electron-hole pairs. The emission bands at around 422, 444 and 463 nm are attributed to presence of $O_2^{\bullet -}$ vacancies. The oxygen vacancies correspond to photoinduced charge traps and adsorption sites, resulting in hindering of the electron-hole recombination and thus, enhancement of the photocatalytic activity [73]. The peak at about 525 nm is attributed to the radiative recombination of mobile electrons with trapped holes. The lowest PL intensity was observed for the samples decorated with GQDs. The observation of the sharp and intensive PL emission spectra for $SrSnO_3$_GQDs_Er, $AgTaO_3$_CQDs and $AgTaO_3$_GQDs_Er was difficult to notice. Similar results for $SrTiO_3$ samples were observed by Umar *et al.* [74].

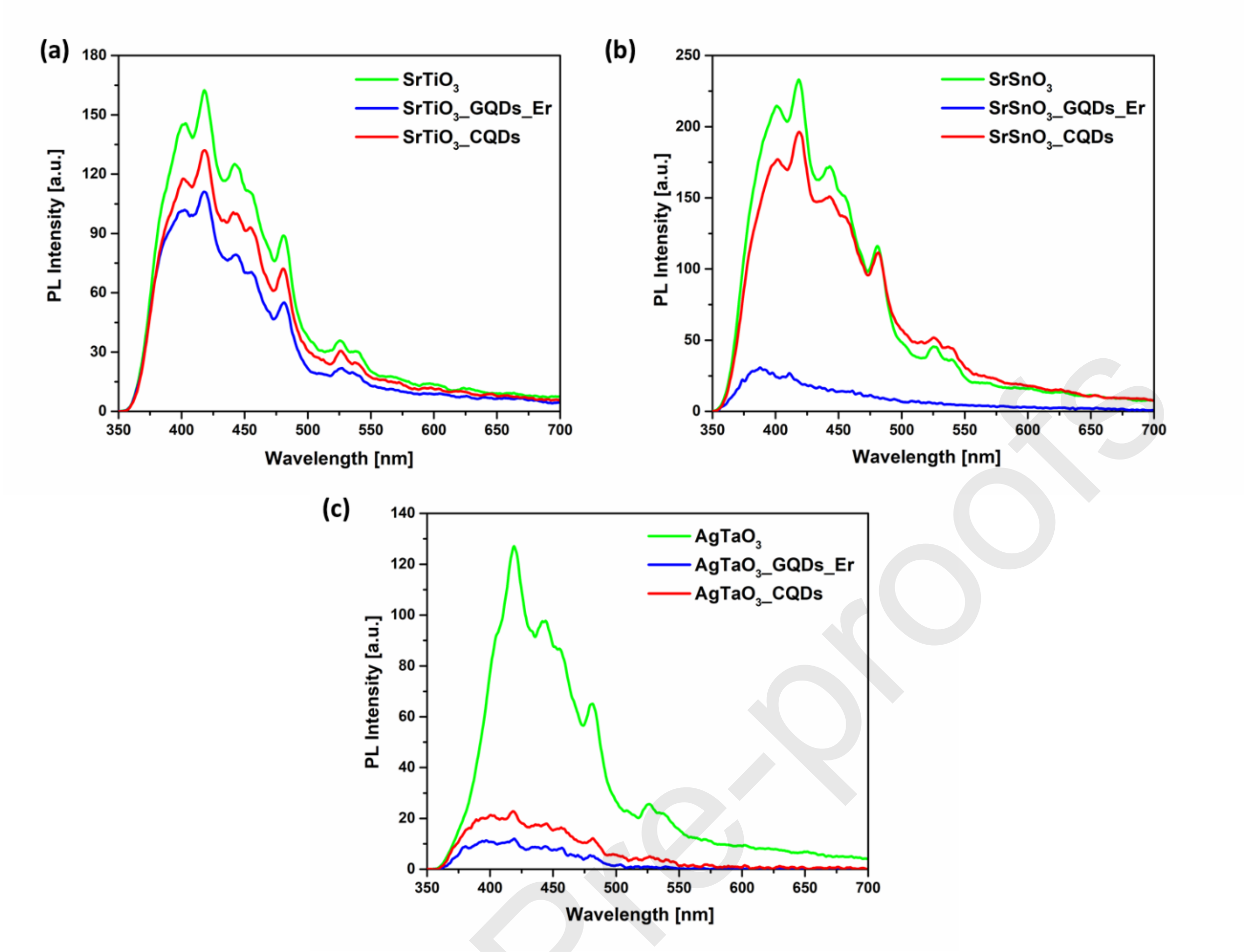

Figure 12 Photoluminescence emission spectra of pristine and of pristine and modified samples: (a) $SrTiO_3$; (b) $AgTaO_3$; (c) $SrSnO_3$.

2.2.6. Photocatalytic activity for toluene degradation in the gas phase

The photocatalytic activity of the prepared samples was evaluated for toluene degradation, and the obtained results are shown in Fig. 13. First, the blank test without photocatalyst was performed to check the direct photolysis of toluene, and *ca.* 12% of toluene was decomposed in such conditions. All pristine samples ($SrSnO_3$, $SrTiO_3$ and $AgTaO_3$) were the least active, showing toluene degradation of 13%, 26% and 14%, respectively. The photoactivity significantly increased (five, two and four times, respectively) after samples' modification with GQDs an Er, reaching the degradation efficiency of 67%, 48% and 57%, respectively. Whereas, the activity enhancement was much lower (3.2, 1.3 and 1.9 times, respectively) after samples' modification with CQDs, reaching 41.3%, 34.1% and 26.1%, respectively. The observed photocatalytic enhancement of $SrSnO_3$_GQDs_Er, $SrTiO_3$_GQDs_Er and $AgTaO_3$_GQDs_Er composites might be attributed to the presence of erbium ion doping since erbium ion can lead to the red shifts of optical adsorption edges which enhanced degradation process. Moreover, it might be expected that the excited electrons reduce the surface Er^{3+} to Er^{2+} upon irradiation. It is worth to mention that those composites have higher photocatalytic efficiency despite lower specific surface area in comparison with pristine perovskites.

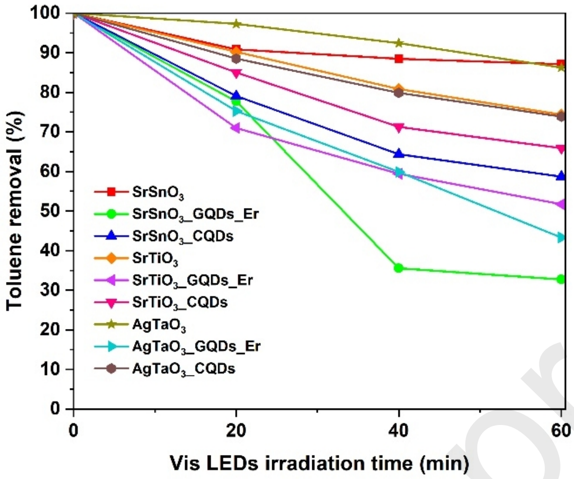

Figure 13 Efficiency of toluene degradation as the function of Vis LEDs irradiation time over pristine and modified: $SrSnO_3$; SrTiO3; $AgTaO_3$.

2.2.7. Photocatalytic activity for phenol degradation in the liquid phase – action spectra

The action spectrum analysis of phenol photodegradation was performed by estimation of the apparent quantum efficiency (AQE) in dependence of irradiation wavelengths (380-600 nm). The AQE was calculated as the ratio of the rate of the electron consumption from the initial rate of benzoquinone (first product of the phenol oxidation) formation to the flux of the incident photons for pristine and modified $SrTiO_3$ and $AgTaO_3$ semiconductors. In the case of pristine and modified $SrSnO_3$, the AQE was estimated on the basis of the initial rates of 1,2,4-benzenetriol formation, which is one of the subsequent products of the phenol decomposition (after benzoquinone) since benzoquinone was oxidized fast (after 20 min of irradiation) into subsequent phenol decomposition products [75]. It was found that AQE values of the modified samples were much higher than that of the pristine samples for all semiconductors ($SrTiO_3$, $SrSnO_3$ and $AgTaO_3$), as shown in in Fig. 14. Moreover, similar to toluene degradation, samples modified with GQDs and erbium were more active than those with CQDs. Two possibilities of higher photoactivity of GQDs/Er-modified samples could be considered, *i.e.*, (i) graphene morphology/properties of carbon or (ii) the erbium presence. It has been reported that graphene could activate titania towards Vis response, as electrons could migrate from photoexcited state of graphene to CB of titania. For example, Wang *et al.* showed Vis-response of both carbon and carbon/graphene modified titania for phenol degradation, but it was found that co-presence of graphene could hindered Vis-activity of carbon-modified samples [76]. Castaneda-Contreras *et al.* attributed the sensitization of titania to visible-light response (a red shift in the band-gap) due to the addition of erbium ions [77]. They proposed that Er ions could transform visible light into UV light (up-conversion) to excite the wide band-gap semiconductor (TiO_2). Although, the bathochromic shift and up-conversion process have not been noticed in the present study but the improved photocatalytic activity is obvious, what has also been observed in the literature [17-19]. It should be pointed out that the characteristic absorption bands for erbium in the third oxidation state at 475, 524 and 655 nm [18] were not detected in this study, probably due to small content of erbium in the samples, the XPS data (Table 2 and on the HR spectra performed for erbium modified samples – Figures: 7, 8 and 9) confirm the erbium presence. Therefore, the possible excitation of semiconductors by erbium could not be excluded. In such case, it is highly possible that GQDs could capture the excited electrons, and thus reduce the recombination of electron-hole pairs [78]. It is well known that electron-hole separation is one of the key factors limiting the efficiency of the photocatalytic process. The photogenerated electrons might migrate from the CB semiconductor *via* GQDs to adsorbed oxygen, forming $O_2^{\bullet -}$ radicals responsible for pollutants' oxidation. Furthermore, the graphene and carbon QDs might couple with $SrTiO_3$, $SrSnO_3$, $AgTaO_3$, and thus also enhance the absorption of the semiconductor in the range of visible light, due to the electronic coupling between states of the graphite-essential GQDs/CQDs and conduction band states of semiconductor. Next, GQDs/CQDs can act as an electron reservoir to trap photogenerated electrons from $SrTiO_3$/$SrSnO_3$/$AgTaO_3$ and promote the separation of photogenerated electron-hole pairs (which is confirmed by PL measurement) [79]. Additionally, literature reports state that lanthanides can also form complexes with various Lewis bases, e.g., acids, amines, aldehydes, alcohols and thiols, by the interaction of listed functional groups with the f-orbitals of the lanthanides [34]. Therefore, inter-corporation of erbium ions in the semiconductor's matrix could provide capabilities to concentrate the organic pollutants at the samples surface [19].

Although, the action spectra do not resemble exactly the respective absorption spectra (Fig. 14 a, b, c), the response under visible-light irradiation confirms Vis activity of the modified samples. It should be pointed out that “absorption spectra” were taken as diffuse reflectance spectra, and thus scattering on large particles of photocatalysts, especially at longer wavelengths was also included in these spectra. In the case of modified $SrTiO_3$ and $SrSnO_3$ samples, the Vis response was observed in the range from 400 nm to 540 nm. In contrast, modified $AgTaO_3$ samples were active till 580 nm, which correlates well with stronger Vis absorption of those samples, probably resulting from the co-presence of metallic silver. It is worth to mention that in case of pristine $SrTiO_3$ and $AgTaO_3$, slight Vis activity was also noticed*, i.e.*, in range from 400 to 460 nm for $SrTiO_3$, and from 400 to 480 nm for $AgTaO_3$. The similar Vis activity has already been reported for other Vis-inactive semiconductors, e.g., titania [80], which could result either from impurities or the oxygen vacancies. In case of pristine $AgTaO_3$, the photoactivity in the visible range of irradiation, might come also from the presence of metallic silver and silver nanoparticles (NPs), which typically show absorption at around 420-500 nm (depending on the size and shape), due to the localized surface plasmon resonance LSPR [81-84]. It was found that the $AgTaO_3$_GQDs_Er sample exhibited the highest Vis photoabsorption among other samples, probably due to the synergistic effect of co-presence of GQDs, Er and metallic silver. Moreover, the content of Ag in this sample (3.71 at.%) was lower than that in pristine $AgTaO_3$ what is in line with results by Wei *et al.,* who reported the highest Vis photoabsorption for the sample with the lowest content of silver [85]. According to the literature, it is well known that the properties of silver NPs influence the position and shape of LSPR peak. It was reported that the broader LSPR is, the higher is the photoactivity of the sample due to the efficient use of all emitted photons [85-87]. Consequently, it has been thought that $AgTaO_3$_GQDs_Er sample demonstrates the highest Vis photoactivity. It is proposed that some silver NPs might be formed during the synthesis process, as confirmed by DRS shape (Figure 14c) and XPS analysis (Table 2, Figure 8). However, the XRD measurements did not revealed the presence of the metallic silver, probably due to low content of silver and the overlapping of the silver peaks with those corresponding to $AgTaO_3$ (Fig. 4c). The broad silver LSPR peak indicates the variety in the size and the shape of silver nanoparticles. Ma *et al.* noted that silver NPs cause significant changes to the absorption spectrum of TiO_2 resulting in high absorbance from 400 nm to entire visible region, which is characteristic for LSPR absorption of spatially confined electrons in Ag NPs [81, 88]. $SrTiO_3$ and $SrSnO_3$ photocatalysts were active till 540 nm and $AgTaO_3$ till 580 nm, and thus it might be concluded that although all photocatalysts might absorb light at much longer wavelengths, those absorption do not result in photocatalyst activation or the concentrations of the phenol by-products are below the detection limit.

To sum up, the obtained perovskites ($SrTiO_3$, $SrSnO_3$ and $AgTaO_3$) are the wide bandgap semiconductors with bandgap larger than 3.0 eV ($SrTiO_3$ – 3.2 eV, $SrSnO_3$ – 3.4 eV and $AgTaO_3$ – 3.4 eV), and thus exhibit superlative properties only under UV irradiation. It was proved (by phenol and toluene photodegradation) that modification by graphene/carbon QDs and erbium caused enhanced photocatalytic properties also under visible range of irradiation (λ>400 nm). Describing in detail, the photocatalytic reaction is initiated after capturing of sunlight by a semiconductor. Consequently, electrons can transfer from valence band (VB) to conduction band (CB) leaving behind holes in the VB. If the photogenerated e^- — h^+ pairs' separation is maintained, the photogenerated carriers can move to the semiconductor surfaces [1, 89, 90]. Then, the oxygen species are formed and the pollutants present on the catalyst surface are decomposed. In this regard, QDs act as an electron acceptor from the semiconductor's conduction band (CB) and the reaction center. Firstly, the coupling of GQDs/CQDs with $SrTiO_3$, $SrSnO_3$ or $AgTaO_3$ enhanced the absorption of perovskites in the range of visible light, probably due to the electronic coupling between states of the graphite-essential QDs (or CQDs) and conduction band states of semiconductors. Secondly, QDs probably can act as an electron reservoir to trap photogenerated electrons from semiconductors and promote the separation of photogenerated electron-holepairs (which is supported by PL measurement) [79]. The differences between GQDs and CQDs, caused by the method of preparation, are observed by the crystalline properties and type of hybridization, *i.e.*, GQDs are composed mainly of sp2 hybridized carbon and they are well crystallized, whereas CQDs possess mainly sp3 hybridized carbon and they are usually amorphous [91]. Accordingly, it is expected that the mobility of charge carriers (*i.e.,* electrons) is much higher on well-crystallized GQDs than that on CQDs, and thus resulting in efficient electron transfer to adsorbed reagents on the photocatalyst surface. Confirmation of this thesis is the higher photocatalytic activity (both in the water and gas phase – phenol and toluene photodegradation) for semiconductors modified with GQDs than for those modified by CQDs. Moreover, the enhanced photocatalytic activity was caused by the addition of erbium. In this case, the excitation under visible irradiation was attributed to both the presence of carbon in a form of QDs as well as modification with erbium.

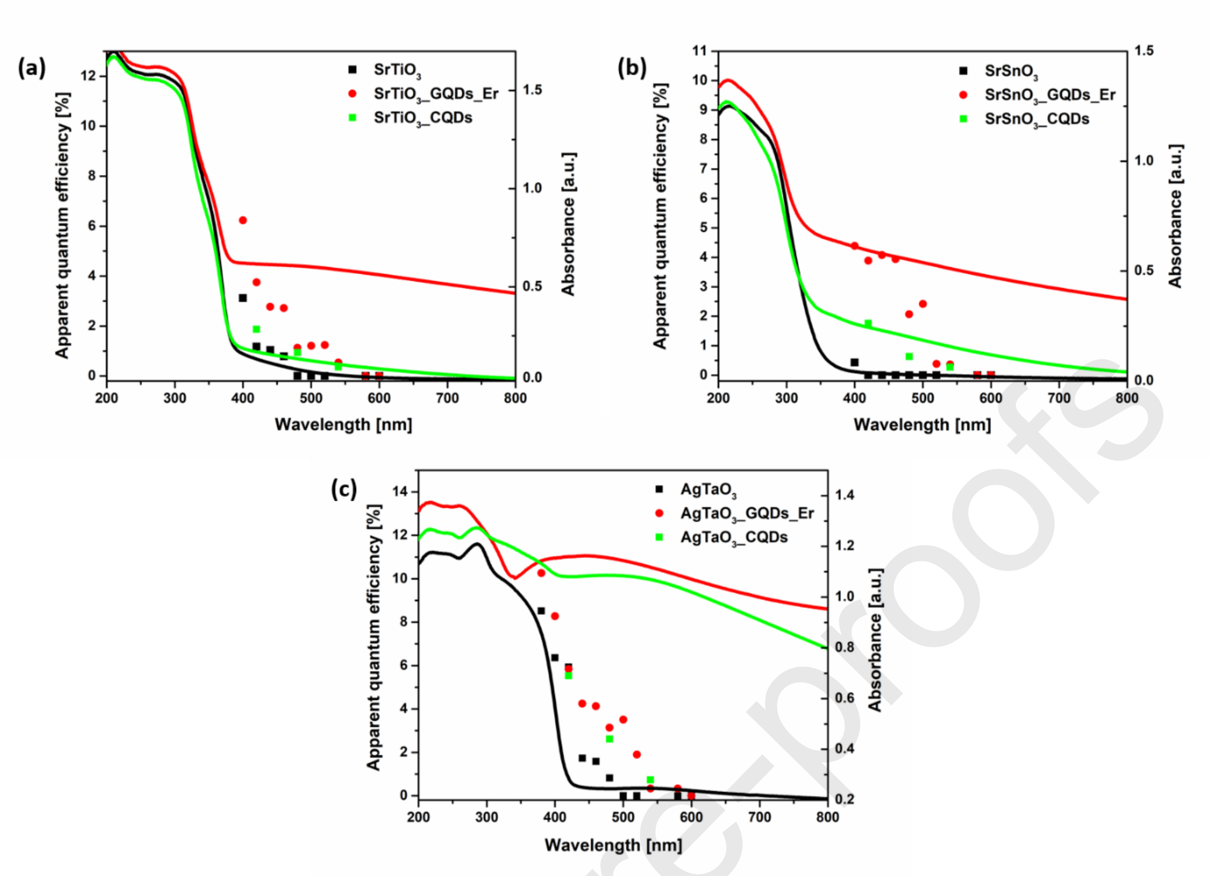

Figure 14 Action spectra for the photocatalytic degradation of phenol in the presence of pristine and modified samples (a) SrTiO$_3$; (b) AgTaO$_3$; (c) SrSnO$_3$ (the lines represent UV-Vis spectra, the dots represents AQE)

2.2.8. Antimicrobial properties

The procedure for determining biocidal activity is shown schematically in the Figure 1 (Experimental Part). Considering the low bactericidal activity of Sr [92, 93], the activities of QDs-modified/unmodified SrSnO$_3$ (Fig. 15a) and SrTiO$_3$ (Fig. 15b) could be recognized by intrinsic activity of oxides and/or photocatalytic activity of the sample. In addition, in the case of SrTiO$_3$, it was found that the modification with GQDs_Er did not enhance the bactericidal activity in the dark (Fig. 15b). As shown in Fig. 15a, pristine SrSnO$_3$ exhibits the activity under Vis. It was also found that the modification with GQDs enhanced the bactericidal activity, although it has been proposed that GQD itself possessed low toxicity [27]. Importantly, although intrinsic (dark) activity of SrSnO$_3$ was not observed, the combination of SrSnO$_3$ and GQDs could facilitate the response in the dark. The bactericidal activity of SrTiO$_3$ and AgTaO$_3$ GQDs were strongly enhanced by the visible light irradiation, due to the photocatalytic biocidal action (Fig. 15b), since it has been proposed that the visible-light (> 420 nm) irradiation itself did not show the bactericidal activity [94]. Moreover, although the silver itself strongly contributed to the bactericidal activity, it is clear that the modification with GQDs enhanced the activity both under Vis and dark condition (Fig. 15c and d). Some reports also suggested that the bactericidal activity of silver-modified semiconductors (mainly titania) was due to the intrinsic activity of silver and photocatalytic reaction (reactive oxygen species) under visible-light irradiation [87, 94-98]. Therefore, it is proposed that the enhanced activity of $AgTaO_3$ under Vis might be due to the plasmonic photocatalysis (Fig. 14c) [99]. Importantly, it has been reported that titania modified with carbon, and both with graphene and carbon did not show the difference in the bactericidal activity, and thus, the existence of graphene seemed not to be responsible for the antibacterial activity [76]. However, in the case of present study, the dark activities of $SrSnO_3$ and $AgTaO_3$ were remarkably enhanced by the modification with GQDs, possibly due to the enhanced direct interaction between the photocatalyst and bacteria [100]. In this sense, a possible reason of the less enhancement of bactericidal activity of $SrTiO_3$ by GQDs in the dark could result from the less carbon content, as shown in Table 2. Summarizing, all GQDs-modified samples showed higher activity than unmodified ones under Vis, possibly due to the enhanced interaction with bacteria and the co-existence of GQDs and H_2O_2 (which might be generated through photocatalytic oxidation of oxygen) [27]

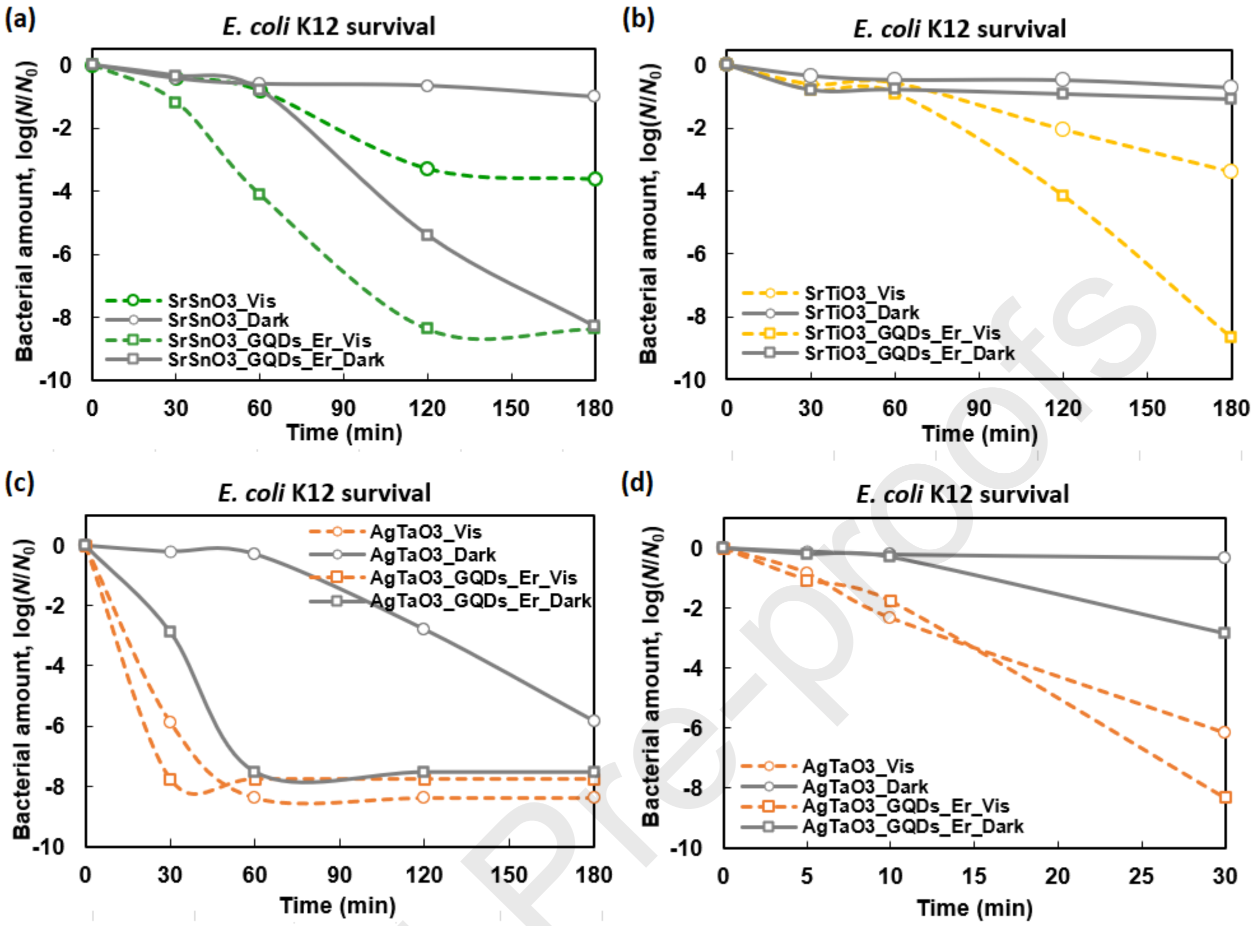

Figure 15 Antimicrobial properties of pristine and modified samples after 180 min of irradiation and in the dark: (a) $SrSnO_3$; (b) $SrTiO_3$; (c) $AgTaO_3$ and (d) $AgTaO_3$ after 30 min of irradiation and in the dark.

Conclusions

The strontium titanate, silver tantalite and strontium stannate perovskites were successfully synthesised *via* solvothermal route at 180°C. The as-prepared samples were modified with carbon quantum dots or graphene quantum dots with 0.5 mol.% of erbium. The morphology analysis showed that the $SrTiO_3$ particles had spherical shape with jagged surface, $SnSrO_3$ formed rods, whereas $AgTaO_3$ were faceted. Although modification of the perovskites by quantum dots lowered their specific surface area, it also resulted in decreased photoluminescence intensity, suggesting the impeded charge carriers' recombination. The lowest photoluminescence intensity was observed for the samples modified by graphene quantum dots and erbium. The higher photocatalytic performance of the modified samples was confirmed by the photocatalytic tests performed under visible-light irradiation for phenol photodegradation in the aqueous phase (estimated apparent quantum efficiency) and toluene decomposition in the gas phase. The mentioned samples exhibited the highest photocatalytic activity in both analysed reaction systems as compared with those modified with carbon quantum dots and the pristine samples (the lowest activity). In this regard, the excitation phenomenon under visible light was attributed to both the presence of carbon in a form of QDs as well as modification with erbium. The higher photocatalytic activity of the perovskites containing graphene QDs and erbium was probably caused by enhanced capturing of the excited electrons, resulting in reduced recombination of the electron-hole pairs, thus improving quantum efficiency. Although GQDs belong also to carbon QDs, and thus having similar properties to other CQDs, such as opto-electronic properties, toxicity, solubility and good photostability, the differences, caused by the method of preparation, are observed by the size, crystalline properties and type of hybridization. As a result, the mobility of charge carriers (*i.e.,* electrons) should be much higher on well-crystallized GQDs than that on CQDs, which resulted in a higher photocatalytic activity.

Taking into account the type of the perovskites, the highest photoactivity under Vis irradiation was observed for the $AgTaO_3$_GQDs_Er sample, probably due to the synergistic effect between GQDs, erbium and metallic silver.

The antimicrobial activity against *Escherichia coli* K12 bacteria confirmed that the co-presence of GQDs and Er resulted in the highest activity. It is expected that the co-existence of GQDs and generated reactive oxygen species (e.g., H_2O_2) could participate in the overall antimicrobial action. Moreover, it was found that GQDs also possessed the bactericidal activity themselves.

It is thought that the data obtained might provide useful information for designing new materials for the efficient removal of chemical and microbiological pollutants under visible irradiation.

Appendix A. Supplementary data

Acknowledgement

Dr Marta Paszkiewicz-Gawron gratefully acknowledge financial support for the research fellowship at Hokkaido University, Institute for Catalysis, Japan, No. PPN/BEK/2018/1/00176 financed by Polish National Agency for Academic Exchange (NAWA) within the Bekker Programme.

The authors also acknowledge the financial support from the National Science Centre within the OPUS 13 programme (grant entitled: “New semiconductor materials for photocatalytic hydrogen generation: mechanism formation in the presence of ionic liquids”), contract No. 2017/25/B/ST8/01119.

The authors thank Prof. Bunsho Ohtani for sound advices and unlimited access to laboratory equipment.

References

[1] M.R. Hoffmann, S.T. Martin, W. Choi, D.W. Bahnemann, Environmental Applications of Semiconductor Photocatalysis, Chemical Reviews, 95 (1995) 69-96.
[2] K. Nakata, A. Fujishima, TiO2 photocatalysis: Design and applications, Journal of Photochemistry and Photobiology C: Photochemistry Reviews, 13 (2012) 169-189.
[3] T. Thompson, J. Yates, Surface Science Studies of the Photoactivation of TiO2 — New Photochemical Processes, Chemical reviews, 106 (2006) 4428-4453.
[4] E. Zarazua, L. Torres-Martínez, D. Sánchez Martínez, C. Gomez, Photocatalytic Performance of Titanates with Formula MTiO3 (M= Fe, Ni, and Co) Synthesized by Solvo-Combustion Method, Materials Research, 20 (2017).
[5] J. Zwara, M. Paszkiewicz-Gawron, J. Łuczak, A. Pancielejko, W. Lisowski, G. Trykowski, A. Zaleska-Medynska, E. Grabowska, The effect of imidazolium ionic liquid on the morphology of Pt nanoparticles deposited on the surface of SrTiO3 and photoactivity of Pt–SrTiO3 composite in the H2 generation reaction, International Journal of Hydrogen Energy, (2019).
[6] C. Gómez-Solís, J. Oliva, L.A. Diaz-Torres, J. Bernal-Alvarado, V. Reyes-Zamudio, A. Abidov, L.M. Torres-Martinez, Efficient photocatalytic activity of MSnO3 (M: Ca, Ba, Sr) stannates for photoreduction of 4-nitrophenol and hydrogen production under UV light irradiation, Journal of Photochemistry and Photobiology A: Chemistry, 371 (2019) 365-373.
[7] H. Kato, A. Kudo, Photocatalytic Water Splitting into H2 and O2 Over Various Tantalate Photocatalysts, Catalysis Today - CATAL TODAY, 78 (2003) 561-569.
[8] P. Kanhere, Z. Chen, A Review on Visible Light Active Perovskite-Based Photocatalysts, Molecules (Basel, Switzerland), 19 (2014) 19995-20022.
[9] H. Kato, H. Kobayashi, A. Kudo, Role of Ag+ in the Band Structures and Photocatalytic Properties of AgMO3 (M: Ta and Nb) with the Perovskite Structure, Cheminform, 34 (2002).
[10] (Invited) Nb-Doped AgTaO3 as a Water-Splitting Photocatalyst Under Visible Light, ECS Meeting Abstracts, (2013).
[11] E.-T. Yun, H.-Y. Yoo, W. Kim, H.-E. Kim, G. Kang, H. Lee, S. Lee, T. Park, C. Lee, J.-H. Kim, J. Lee, Visible-light-induced activation of periodate that mimics dye-sensitization of TiO2: Simultaneous decolorization of dyes and production of oxidizing radicals, Applied Catalysis B: Environmental, 203 (2017) 475-484.
[12] E.M. Samsudin, S.B.A. Hamid, J.C. Juan, W.J. Basirun, G. Centi, Enhancement of the intrinsic photocatalytic activity of TiO2 in the degradation of 1,3,5-triazine herbicides by doping with N,F, Chemical Engineering Journal, 280 (2015) 330-343.
[13] Y. Park, N.J. Singh, K.S. Kim, T. Tachikawa, T. Majima, W. Choi, Fullerol–Titania Charge-Transfer-Mediated Photocatalysis Working under Visible Light, Chemistry – A European Journal, 15 (2009) 10843-10850.
[14] R. Lamba, A. Umar, S.K. Mehta, S.K. Kansal, Enhanced visible light driven photocatalytic application of Ag2O decorated ZnO nanorods heterostructures, Separation and Purification Technology, 183 (2017) 341-349.

[15] A. Gołąbiewska, A. Zielińska-Jurek, A. Zaleska, Characterization of TiO2 modified with bimetallic Ag/Au nanoparticles obtained in microemulsion system, Journal of Advanced Oxidation Technologies, 15 (2012) 71-77.
[16] J. Reszczynska, A. Iwulska, G. Sliwinski, A. Zaleska, Characterization and photocatalytic activity of rare earth metal-doped titanium dioxide, Physicochem. Probl. Miner. Process, 48 (2012) 201-208.
[17] J. Reszczyńska, T. Grzyb, J.W. Sobczak, W. Lisowski, M. Gazda, B. Ohtani, A. Zaleska, Lanthanide co-doped TiO2: The effect of metal type and amount on surface properties and photocatalytic activity, Applied Surface Science, 307 (2014) 333-345.
[18] J. Reszczyńska, T. Grzyb, Z. Wei, M. Klein, E. Kowalska, B. Ohtani, A. Zaleska-Medynska, Photocatalytic activity and luminescence properties of RE3+–TiO2 nanocrystals prepared by sol–gel and hydrothermal methods, Applied Catalysis B: Environmental, 181 (2016) 825-837.
[19] J. Reszczyńska, T. Grzyb, J.W. Sobczak, W. Lisowski, M. Gazda, B. Ohtani, A. Zaleska, Visible light activity of rare earth metal doped (Er3+, Yb3+ or Er3+/Yb3+) titania photocatalysts, Applied Catalysis B: Environmental, 163 (2015) 40-49.
[20] J. Łuczak, M. Paszkiewicz-Gawron, M. Długokęcka, W. Lisowski, E. Grabowska, S. Makurat, J. Rak, A. Zaleska-Medynska, Visible light photocatalytic activity of ionic liquid-TiO2 spheres: effect of the ionic liquid's anion structure, ChemCatChem, 9 (2017) 4377 – 4388.
[21] M. Miodyńska, A. Mikolajczyk, B. Bajorowicz, J. Zwara, T. Klimczuk, W. Lisowski, G. Trykowski, H. Pinto, A. Zaleska-Medynska, Urchin-like TiO2 structures decorated with lanthanide-doped Bi2S3 quantum dots to boost hydrogen photogeneration performance, Applied Catalysis B: Environmental, (2020) 118962.
[22] E. Galdiero, A. Siciliano, V. Maselli, R. Gesuele, M. Guida, D. Fulgione, S. Galdiero, L. Lombardi, A. Falanga, An integrated study on antimicrobial activity and ecotoxicity of quantum dots and quantum dots coated with the antimicrobial peptide indolicidin, International Journal of Nanomedicine, 2016:11 (2016) 4199—4211.
[23] S. Sharma, A. Umar, S. Sood, S. Mehta, S. Kansal, Photoluminescent C-dots: An overview on the recent development in the synthesis, physiochemical properties and potential applications, Journal of Alloys and Compounds, 748 (2018).
[24] S. Campuzano, P. Yáñez-Sedeño, J. Pingarrón, Carbon Dots and Graphene Quantum Dots in Electrochemical Biosensing, Nanomaterials, 9 (2019) 634.
[25] M. Pedrero, S. Campuzano, J. Pingarrón, Electrochemical (Bio)sensing of Clinical Markers Using Quantum Dots, Electroanalysis, (2016).
[26] M. Meziani, X. Dong, L. Zhu, L. Jones, G. Lecroy, F. Yang, S. Wang, P. Wang, Y. Zhao, L. Yang, R. Tripp, S. Yaping, Visible Light-Activated Bactericidal Functions of Carbon "Quantum" Dots, ACS applied materials & interfaces, 8 (2016).
[27] H. Sun, N. Gao, K. Dong, J. Ren, X. Qu, Graphene Quantum Dots-Band-Aids Used for Wound Disinfection, ACS nano, 8 (2014).
[28] R. Gill, M. Zayats, I. Willner, Semiconductor Quantum Dots for Bioanalysis, Angewandte Chemie International Edition, 47 (2008) 7602-7625.
[29] M. Ahmaruzzaman, D. Mohanta, A. Nath, Environmentally benign fabrication of SnO2-CNT nanohybrids and their multifunctional efficiency as an adsorbent, catalyst and antimicrobial agent for water decontamination, Scientific Reports, 9 (2019).
[30] H.L. Huang, M.-T. Tsai, Y.-J. Lin, Y.-Y. Chang, Antibacterial and biological characteristics of tantalum oxide coated titanium pretreated by plasma electrolytic oxidation, Thin Solid Films, 688 (2019).
[31] T. Matsunaga, R. Tomoda, T. Nakajima, H. Wake, Photoelectrochemical sterilization of microbial cells by semiconductor powders, FEMS Microbiology Letters, 29 (1985) 211-214.
[32] T. Matsunaga, R. Tomoda, T. Nakajima, N. Nakamura, T. Komine, Continuous-sterilization system that uses photosemiconductor powders. [Escherichia coli], Appl. Environ. Microbiol., (1988).
[33] A. Markowska-Szczupak, K. Ulfig, A.W. Morawski, The application of titanium dioxide for deactivation of bioparticulates: An overview, Catalysis Today, 169 (2011) 249-257.

[34] K.T. Ranjit, I. Willner, S.H. Bossmann, A.M. Braun, Lanthanide Oxide-Doped Titanium Dioxide Photocatalysts: Novel Photocatalysts for the Enhanced Degradation of p-Chlorophenoxyacetic Acid, Environmental Science & Technology, 35 (2001) 1544-1549.
[35] C.-H. Liang, M. Hou, S.-G. Zhou, F.-b. Li, C.-S. Liu, T. Liu, Y.-X. Gao, X.-G. Wang, J.-L. Lü, The effect of erbium on the adsorption and photodegradation of orange I in aqueous Er3+-TiO2 suspension, Journal of hazardous materials, 138 (2007) 471-478.
[36] Y. Zhang, H. Zhang, Y. Xu, Y. Wang, Significant effect of lanthanide doping on the texture and properties of nanocrystalline mesoporous TiO2, Journal of Solid State Chemistry, 177 (2004) 3490-3498.
[37] A. Weber, A. Grady, R. Koodali, Lanthanide modified semiconductor photocatalysts, Catal. Sci. Technol., 2 (2012) 683-693.
[38] S. Weng, D. Liang, H. Qiu, Z. Liu, Z. Lin, Z. Zheng, A. Liu, W. Chen, X. Lin, A unique turn-off fluorescent strategy for sensing dopamine based on formed polydopamine (pDA) using graphene quantum dots (GQDs) as fluorescent probe, Sensors and Actuators B: Chemical, 221 (2015) 7-14.
[39] P. Chen, F. Wang, Z.-F. Chen, Q. Zhang, Y. Su, L. Shen, K. Yao, Y. Liu, Z. Cai, W. Lv, G. Liu, Study on the photocatalytic mechanism and detoxicity of gemfibrozil by a sunlight-driven TiO2/carbon dots photocatalyst: The significant roles of reactive oxygen species, Applied Catalysis B: Environmental, 204 (2017) 250-259.
[40] P. E., Larson, M. A., Kelly, U.S. patent 5,990,476A

(November 23, 1999), JP patent P3616714B2 (February 2, 2005), and EP patent

0848247B1 (July 3, 2002).
[41] M. Nischk, P. Mazierski, M. Gazda, A. Zaleska, Ordered TiO2 nanotubes: The effect of preparation parameters on the photocatalytic activity in air purification process, Applied Catalysis B: Environmental, 144 (2014) 674-685.
[42] A. Markowska-Szczupak, P. Rokicka, K. Wang, M. Endo, W.A. Morawski, E. Kowalska, Photocatalytic Water Disinfection under Solar Irradiation by d-Glucose-Modified Titania, Catalysts, 8 (2018).
[43] Q. Liu, B. Guo, Z. Rao, B. Zhang, J.R. Gong, Strong Two-Photon-Induced Fluorescence from Photostable, Biocompatible Nitrogen-Doped Graphene Quantum Dots for Cellular and Deep-Tissue Imaging, Nano Letters, 13 (2013) 2436-2441.
[44] D. Li, D. Han, S.-N. Qu, L. Liu, P.-T. Jing, D. Zhou, W.-Y. Ji, X.-Y. Wang, T.-F. Zhang, D.-Z. Shen, Supra-(carbon nanodots) with a strong visible to near-infrared absorption band and efficient photothermal conversion, Light: Science & Applications, 5 (2016) e16120-e16120.
[45] Z. Wang, F. Yuan, X. Li, Y. Li, H. Zhong, L. Fan, S. Yang, 53% Efficient Red Emissive Carbon Quantum Dots for High Color Rendering and Stable Warm White-Light-Emitting Diodes, Advanced Materials, 29 (2017) 1702910.
[46] D. Konstantinos, Carbon Quantum Dots: Surface Passivation and Functionalization, Current Organic Chemistry, 20 (2016) 682-695.
[47] Y.-P. Sun, B. Zhou, Y. Lin, W. Wang, K.A.S. Fernando, P. Pathak, M.J. Meziani, B.A. Harruff, X. Wang, H. Wang, P.G. Luo, H. Yang, M.E. Kose, B. Chen, L.M. Veca, S.-Y. Xie, Quantum-Sized Carbon Dots for Bright and Colorful Photoluminescence, Journal of the American Chemical Society, 128 (2006) 7756-7757.
[48] F. Arcudi, L. Đorđević, M. Prato, Synthesis, Separation, and Characterization of Small and Highly Fluorescent Nitrogen-Doped Carbon NanoDots, Angewandte Chemie International Edition, 55 (2016) 2107-2112.
[49] Y. Li, X. Zhong, A.E. Rider, S.A. Furman, K. Ostrikov, Fast, energy-efficient synthesis of luminescent carbon quantum dots, Green Chemistry, 16 (2014) 2566-2570.
[50] A. Kouloumpis, E. Thomou, N. Chalmpes, K. Dimos, K. Spyrou, A.B. Bourlinos, I. Koutselas, D. Gournis, P. Rudolf, Graphene/Carbon Dot Hybrid Thin Films Prepared by a Modified Langmuir–Schaefer Method, ACS Omega, 2 (2017) 2090-2099.

[51] Q. Hu, M.C. Paau, Y. Zhang, X. Gong, L. Zhang, D. Lu, Y. Liu, Q. Liu, J. Yao, M.M.F. Choi, Green synthesis of fluorescent nitrogen/sulfur-doped carbon dots and investigation of their properties by HPLC coupled with mass spectrometry, RSC Advances, 4 (2014) 18065-18073.
[52] X. Wen, P. Yu, Y.-R. Toh, X. Ma, J. Tang, On the upconversion fluorescence in carbon nanodots and graphene quantum dots, Chemical Communications, 50 (2014) 4703-4706.
[53] A. Barati, M. Shamsipur, H. Abdollahi, A misunderstanding about upconversion luminescence of carbon quantum dots, Journal of the Iranian Chemical Society, 12 (2015) 441-446.
[54] Y. Cai, X. Piao, W. Gao, Z. Zhang, E. Nie, Z. Sun, Large-scale and facile synthesis of silver nanoparticles via a microwave method for a conductive pen, RSC Advances, 7 (2017) 34041-34048.
[55] J. Zhang, Y. Li, Y. Zhang, M. Chen, L. Wang, C. Zhang, H. He, Effect of Support on the Activity of Ag-based Catalysts for Formaldehyde Oxidation, Scientific Reports, 5 (2015) 12950.
[56] C.L. Liang, K. Zhong, M. Liu, L. Jiang, S.K. Liu, D.D. Xing, H.Y. Li, Y. Na, W.X. Zhao, Y.X. Tong, P. Liu, Synthesis of morphology-controlled silver nanostructures by electrodeposition, Nano-Micro Letters, 2 (2010) 6-10.
[57] M. Vanaja, G. Annadurai, Coleus aromaticus leaf extract mediated synthesis of silver nanoparticles and its bactericidal activity, Applied Nanoscience, 3 (2013) 217-223.
[58] V. Štengl, D. Popelková, P. Vláčil, TiO2–Graphene Nanocomposite as High Performace Photocatalysts, The Journal of Physical Chemistry C, 115 (2011) 25209-25218.
[59] K. Kim, S. Kang, B. Kwak, M. Kang, Enhancement of Hydrogen Production from MeOH/H2O Photo-Splitting Using Micro-/Nano-Structured SrSnO3/TiO2 Composite Catalysts, Journal of nanoscience and nanotechnology, 14 (2014) 9198-9205.
[60] A.V. Naumkin, A. Kraut-Vass, S.W. Gaarenstroom, C.J. Powell, NIST X-ray Photoelectron Spectroscopy Database 20, Version 4.1, 2012.
[61] E. Grabowska, M. Marchelek, T. Klimczuk, W. Lisowski, A. Zaleska-Medynska, TiO2/SrTiO3 and SrTiO3 microspheres decorated with Rh, Ru or Pt nanoparticles: Highly UV–vis responsible photoactivity and mechanism, Journal of Catalysis, 350 (2017) 159-173.
[62] M. Oku, K. Wagatsuma, S. Kohiki, Ti 2p and Ti 3p X-ray photoelectron spectra for TiO2, SrTiO3 and BaTiO3, Physical Chemistry Chemical Physics, 1 (1999) 5327-5331.
[63] M. Li, J. Zhang, W. Dang, S.K. Cushing, D. Guo, N. Wu, P. Yin, Photocatalytic hydrogen generation enhanced by band gap narrowing and improved charge carrier mobility in AgTaO3 by compensated co-doping, Physical Chemistry Chemical Physics, 15 (2013) 16220-16226.
[64] T. Alammar, I. Hamm, V. Grasmik, M. Wark, A.-V. Mudring, Microwave-Assisted Synthesis of Perovskite SrSnO3 Nanocrystals in Ionic Liquids for Photocatalytic Applications, Inorganic Chemistry, 56 (2017) 6920-6932.
[65] F. Rabuffetti, H.-S. Kim, J. Enterkin, Y. Wang, C. Lanier, L. Marks, K. Poeppelmeier, P. Stair, Synthesis-Dependent First-Order Raman Scattering in SrTiO 3 Nanocubes at Room Temperature, Chemistry of Materials - CHEM MATER, 20 (2008) 5628-5635.
[66] W. Shi, H. Fan, S. Ai, L.-S. Zhu, Preparation of fluorescent graphene quantum dots from humic acid for bioimaging application, New J. Chem., 39 (2015).
[67] T. Shen, Q. Wang, Z. Guo, J. Kuang, W. Cao, Hydrothermal synthesis of carbon quantum dots using different precursors and their combination with TiO 2 for enhanced photocatalytic activity, Ceramics International, 44 (2018).
[68] G.E. Kugel, M.D. Fontana, M. Hafid, K. Roleder, A. Kania, M. Pawelczyk, A Raman study of silver tantalate (AgTaO3) and its structural phase transition sequence, Journal of Physics C: Solid State Physics, 20 (1987) 1217-1230.
[69] T. Alammar, I. Hamm, V. Grasmik, M. Wark, A.-V. Mudring, Microwave-Assisted Synthesis of Perovskite SrSnO 3 Nanocrystals in Ionic Liquids for Photocatalytic Applications, Inorganic Chemistry, 56 (2017).
[70] M. Singh, N. Karan, R. Katiyar, J. Scott, H. Jang, New phase transitions in ceramic SrSnO3: Raman scattering analysis and differential thermal analysis, Journal of Physics: Condensed Matter, 20 (2008) 055210.

[71] M. Tarrida, H. Larguem, M. Madon, Structural investigations of (Ca,Sr)ZrO3 and Ca(Sn,Zr)O3 perovskite compounds, Physics and Chemistry of Minerals, 36 (2009).
[72] M. Alves, M. Rodrigues, S. Lima, P. Pizani, J. Espinosa, E. Longo, L. Soledade, A. Souza, I. Santos, Influence of synthesis conditions on carbonate entrapment in perovskite SrSnO3, Materials Letters, 63 (2009) 118-120.
[73] M. Kong, Y. Li, X. Chen, T. Tian, P. Fang, F. Zheng, X. Zhao, Tuning the Relative Concentration Ratio of Bulk Defects to Surface Defects in TiO2 Nanocrystals Leads to High Photocatalytic Efficiency, Journal of the American Chemical Society, 133 (2011) 16414-16417.
[74] U.K.N. Din, M. Mat Salleh, H. Aziz, A. Ali Umar, Composition dependence of photoluminescence properties of poly(9,9-di-n-hexylfluorenyl-2,7-diyl) with perovskite-structured SrTiO3 nanocomposites, Superlattices and Microstructures, 93 (2016) 153-156.
[75] M. Diak, M. Klein, T. Klimczuk, W. Lisowski, H. Remita, A. Zaleska-Medynska, E. Grabowska, Photoactivity of decahedral TiO2 loaded with bimetallic nanoparticles: Degradation pathway of phenol-1-13C and hydroxyl radical formation, Applied Catalysis B: Environmental, 200 (2017) 56-71.
[76] Kunlei Wang , Maya Endo-Kimura , Raphaëlle Belchi , Dong Zhang , Aurelie Habert , Johann Bouclé , Bunsho Ohtani , E. Kowalska, N.a. Herlin-Boime, Carbon/Graphene-Modified Titania with Enhanced Photocatalytic Activity under UV and Vis Irradiation, Materials, 12 (2019).
[77] J. Castañeda-Contreras, V.F. Marañón-Ruiz, R. Chiu-Zárate, H. Pérez-Ladrón de Guevara, R. Rodriguez, C. Michel-Uribe, Photocatalytic activity of erbium-doped TiO2 nanoparticles immobilized in macro-porous silica films, Materials Research Bulletin, 47 (2012) 290-295.
[78] B. Quan, W. Liu, Y. Liu, Y. Zheng, G. Yang, G. Ji, Quasi-noble-metal graphene quantum dots deposited stannic oxide with oxygen vacancies: Synthesis and enhanced photocatalytic properties, Journal of Colloid and Interface Science, 481 (2016) 13-19.
[79] A. Qu, H. Xie, X. Xu, Y. Zhang, S. Wen, Y. Cui, High quantum yield graphene quantum dots decorated TiO2 nanotubes for enhancing photocatalytic activity, Applied Surface Science, 375 (2016) 230-241.
[80] Z. Wei, M. Janczarek, M. Endo, K. Wang, A. Balčytis, A. Nitta, M.G. Méndez-Medrano, C. Colbeau-Justin, S. Juodkazis, B. Ohtani, E. Kowalska, Noble metal-modified faceted anatase titania photocatalysts: Octahedron versus decahedron, Applied Catalysis B: Environmental, 237 (2018) 574-587.
[81] M. Diak, E. Grabowska, A. Zaleska, Synthesis, characterization and photocatalytic activity of noble metal-modified TiO2 nanosheets with exposed {001} facets, Applied Surface Science, 347 (2015) 275-285.
[82] T. Ghodselahi, T. Neishaboorynejad, S. Arsalani, Fabrication LSPR sensor chip of Ag NPs and their biosensor application based on interparticle coupling, Applied Surface Science, 343 (2015) 194-201.
[83] M. Klein, J. Nadolna, A. Gołąbiewska, P. Mazierski, T. Klimczuk, H. Remita, A. Zaleska-Medynska, The effect of metal cluster deposition route on structure and photocatalytic activity of mono- and bimetallic nanoparticles supported on TiO2 by radiolytic method, Applied Surface Science, 378 (2016) 37-48.
[84] E. Kowalska, M. Janczarek, L. Rosa, S. Juodkazis, B. Ohtani, Mono- and bi-metallic plasmonic photocatalysts for degradation of organic compounds under UV and visible light irradiation, Catalysis Today, 230 (2014) 131-137.
[85] Z. Wei, M. Janczarek, M. Endo, C. Colbeau-Justin, B. Ohtani, E. Kowalska, Silver-modified octahedral anatase particles as plasmonic photocatalyst, Catalysis Today, 310 (2018) 19-25.
[86] E. Kowalska, O. Prieto, R. Abe, B. Ohtani, Visible-light-induced photocatalysis through surface Plasmon excitation of gold on titania surfaces, Physical chemistry chemical physics : PCCP, 12 (2010) 2344-2355.
[87] E. Kowalska, Z. Wei, B. Karabiyik, A. Herissan, M. Janczarek, M. Endo, A. Markowska-Szczupak, H. Remita, B. Ohtani, Silver-modified titania with enhanced photocatalytic and antimicrobial properties under UV and visible light irradiation, Catalysis Today, 252 (2015) 136-142.
[88] J. Ma, X. Guo, Y. Zhang, H. Ge, Catalytic performance of TiO2@Ag composites prepared by modified photodeposition method, Chemical Engineering Journal, 258 (2014) 247-253.

[89] Fujishima A., H. K., Electrochemical photolysis of water at a semiconductor electrode, Nature, 238 (1972) 37-38.
[90] A. Fujishima, T.N. Rao, D.A. Tryk, Titanium dioxide photocatalysis, Journal of Photochemistry and Photobiology C: Photochemistry Reviews, 1 (2000) 1-21.
[91] A. Cayuela, M.L. Soriano, C. Carrillo-Carrión, M. Valcárcel, Semiconductor and carbon-based fluorescent nanodots: the need for consistency, Chemical Communications, 52 (2016) 1311-1326.
[92] S. Alghool, H. El-Halim, A. Dahshan, Synthesis, spectroscopic thermal and biological activity studies on azo-containing Schiff base dye and its Cobalt(II), Chromium(III) and Strontium(II) complexes, Journal of Molecular Structure, 983 (2010) 32-38.
[93] D. Brauer, N. Karpukhina, G. Kedia, A. Bhat, R. Law, I. Radecka, R. Hill, Bactericidal strontium-releasing injectable bone cements based on bioactive glasses, Journal of the Royal Society, Interface / the Royal Society, 10 (2013) 20120647.
[94] M. Endo, M. Janczarek, Z. Wei, K. Wang, A. Markowska-Szczupak, B. Ohtani, E. Kowalska, Bactericidal Properties of Plasmonic Photocatalysts Composed of Noble Metal Nanoparticles on Faceted Anatase Titania, Journal of Nanoscience and Nanotechnology, 19 (2019) 442-452.
[95] S. Rtimi, O. Baghriche, R. Sanjines, C. Pulgarin, M. Bensimon, J. Kiwi, TiON and TiON-Ag sputtered surfaces leading to bacterial inactivation under indoor actinic light, Journal of Photochemistry and Photobiology A: Chemistry, 256 (2013) 52-63.
[96] Z. Wei, M. Endo, K. Wang, E. Charbit, A. Markowska-Szczupak, B. Ohtani, E. Kowalska, Noble metal-modified octahedral anatase titania particles with enhanced activity for decomposition of chemical and microbiological pollutants, Chemical Engineering Journal, 318 (2017) 121-134.
[97] M. Endo, Z. Wei, K. Wang, B. Karabiyik, K. Yoshiiri, P. Rokicka, B. Ohtani, A. Markowska-Szczupak, E. Kowalska, Noble metal-modified titania with visible-light activity for the decomposition of microorganisms, Beilstein Journal of Nanotechnology, 9 (2018) 829-841.
[98] M. Endo-Kimura, M. Janczarek, Z. Bielan, D. Zhang, K. Wang, A. Markowska-Szczupak, E. Kowalska, Photocatalytic and Antimicrobial Properties of Ag2O/TiO2 Heterojunction, ChemEngineering, 3 (2019).
[99] M. Endo-Kimura, E. Kowalska, Plasmonic Photocatalysts for Microbiological Applications, Catalysts, 10 (2020).
[100] C.-L. Cheng, D.-S. Sun, W.-C. Chu, Y.-H. Tseng, H.-C. Ho, J.-B. Wang, P.-H. Chung, J.-H. Chen, P.-J. Tsai, N.-T. Lin, M.-S. Yu, H.-H. Chang, The effects of the bacterial interaction with visible-light responsive titania photocatalyst on the bactericidal performance, Journal of Biomedical Science, 16 (2009) 7.

Graphical abstract